ELASTIC VISCO-PLASTIC MODEL OF STEEL SOLIDIFICATION
WITH LOCAL DAMAGE AND FAILURE

BY

ARAVIND MURALI

THESIS

Submitted in partial fulfillment of the requirements
for the degree of Master of Science in Mechanical Engineering
in the Graduate College of the
University of Illinois Urbana-Champaign, 2022

Urbana, Illinois

Adviser:

Professor Brian G. Thomas

ABSTRACT

A nonlinear elastic visco-plastic thermo-mechanical steel microstructure model is coupled with a Gurson-Tvergaard-Needleman (GTN) model to predict local damage and failure in the columnar solidification zone of a steel casting. The new model operates on two scales - a micro-scale model of a representative unit cell in the columnar zone as well as a macro-scale model of a tensile specimen to match micro-scale observations with experiments. The micro-scale model aims to investigate inter-granular embrittlement at intermediate temperatures during solidification processes. This embrittlement occurs due to pro-eutectoid ferrite film formation and precipitation at the prior austenite grain boundaries. This behavior of the unit cell is then mapped onto macro-model tensile specimens to measure reduction in ductility. The effects of ferrite films and test temperature are studied by calculating the micro-strains, macro-strains and void fractions at which cracks begin to form during the process. The developed model shows good agreement with experimental data. It is then further used to study the impact of the presence of the ferrite films, temperature of the steel as well different types of loading on the micro-scale mechanical behavior which depends on the particular location on the cast strand. The presence of ferrite films at the austenite grain boundaries is a significant driver of intermediate-temperature embrittlement as predicted by the model. This is further exacerbated by increase in test temperature. An increase in temperature causes an overall reduction in the strength of the steel but also increases the strength of the grain matrix in comparison to the strength of the ferrite films. This difference in strength between the grain matrix and grain boundary causes further strain concentration leading to premature embrittlement. This temperature effect has a ten-fold greater impact on embrittlement compared to the different types of loading on the micro-scale.

ACKNOWLEDGMENTS

This project would not have been possible without the support of many people. Many thanks to my adviser, Brian G. Thomas, for the long discussions during the course of the development as well as for reading my numerous revisions and helped make some sense of everything. I also thank the Continuous Casting Consortium Members (ABB, ArcelorMittal, Baosteel, Magnesita Refractories, Nippon Steel and Sumitomo Metal Corp., Nucor Steel, Postech/ Posco, Severstal, SSAB, Tata Steel, ANSYS/ Fluent) without whose monetary support; this project would not be possible. I would also like to thank Dr. Seid Koric, and Dr. Lance Hibbeler for their timely guidance during the course of this project without which this work would not have been possible.

Finally, thanks to Sindhuja, my parents, and numerous friends who have endured this long process with me always offering me their support and love.

CONTENTS

CHAPTER 1: INTRODUCTION

Steel is an important engineering material that is ubiquitous in day-to-day life. The combined advantages of high strength and low costs have made it a critical component in the development of infrastructure and economy of a nation. It is in the best interest of development that such a critical material be produced with the least amount of defects. One area of steel processing which is prone to issues with defects has been the high temperature processing of steel and associated ductility troughs. Although modern analysis techniques and computational models have been applied as a powerful tool to predict stress and deformation during steel processing, thereby minimizing the formation of associated defects; little previous work has been done to predict steel ductility, specifically towards understanding the high temperature ductility troughs using fundamental computational models.

The current work is in the area continuous casting of steel. Continuous casting of steel accounts for nearly 90% of the world's production of steel. The actual process has a complex interplay of stress, fluid flow and metallurgy, which have critical effects on the final quality of steel produced. There is an ongoing effort around the world in trying to understand and control the process such that the undesirable effects that lead to formation of defects in the process are mitigated. Looking to contribute towards this effort, the ultimate objective of the current work is to develop a working methodology to link the microstructure to the macroscale physical properties such as ductility that lead to formation of casting defects such as longitudinal or transverse cracks and thus are of critical importance to the steel casting process. In particular, the current work can help understand how the grain features (such as grain size and shape, phases, and precipitates) have an effect on the overall quality of the steel produced (properties of steel such as ductility). These models working in unison with knowledge already available in the form of modeling the steel alloy composition and the cooling history as well as mold process conditions would help reduce these defects from occurring and ensuring that the best quality of steel is being produced.

The specific objective of this project is to obtain a methodology to model the effect of external stresses, as well as internal microstructure of grains on the macroscale steel ductility and the formation of sub-surface transverse cracks. This model developed here will help to understand the mechanism of a developing crack, at intermediate-temperatures (1200˚C-800˚C), along the grain boundaries (inter-granular cracks). In particular, the current model will attempt to answer the question of how weak the region around the grain boundary has to be in comparison to the grain, for a crack to nucleate and propagate along the grain boundary, rather than inside the grain. This is achieved through a thermal-mechanical model using ABAQUS to conduct an uncoupled stress analysis of the microstructure with an elastic-perfectly plastic material and a Gurson [29] failure model for void nucleation and crack formation. The present work thus tries to obtain a methodology to model and analyze these micro-scale phenomena with an objective to connect this to macro-scale observations in lab-scale tensile specimens or, more importantly, in the solidifying steel slab in the commercial continuous casting process.

The scope of the current project leaves out the effect of anisotropy of the grains and its effect on the stress concentration on the grain boundaries due to slipping and sliding between the grains. This in effect leaves out the formation of wedge type (‘W’) cracks [2]. This is because these occur in the grain boundaries attributed to the slipping action of grain boundaries. As an initial step towards this ambitious objective, the current model also does not incorporate the effects of grain growth and coarsening and aims to overcome this by evaluating mechanical behavior at sufficiently-short time intervals that the geometric dimensions of the grain remain almost constant for the duration of analysis. For the same reason, the effect of solidification is not incorporated either, although it is important for analysis of thermal stresses.

The present model is an off-line model that can help researchers to understand the underlying phenomena that cause certain adverse effects and undesirable sub-surface transverse cracks in steel. In future, a more comprehensive version of this model, including the effects of precipitate size and distribution, would help to understand the effect that these precipitates have on the properties of steel being produced (strength, brittleness or ductility). Furthermore, the ultimate goal is to extend this to a process model that can be used by the process engineer in a steel plant to understand and remediate problems that affect the accompanying defects in the real process that affect steel quality, such as the formation of cracks, hot tears and breakout shells.

1.1: BACKGROUND

Figure.1.1 shows a schematic of the continuous casting process. The objective of the process is to cast molten steel into slabs of necessary dimensions. The process starts with molten steel that is being poured into a tundish from a ladle. The tundish serves as a temporary holding pen for the molten steel so that there are no variations to the flow of the steel during the process of switching ladles.

The tundish also serves the purpose of removing undesirable impurities using separation techniques. The molten steel then enters the mold through a submerged entry nozzle. This nozzle helps avoid the unnecessary disturbances that occur in the flow of the steel from the tundish to the mold, due to turbulence. The nozzle also helps protect the steel from atmospheric oxidation and direct the flow of molten steel in the mold. The steel then starts solidifying inside the mold while at the same time moving down at the casting speed due to the force applied by the drive rolls. Rolls support the shell after it exits the mold and moves down through the secondary cooling zones, where it is spray cooled with water until completely solidified and cooled. Then the slab is cut off into appropriate lengths using a torch.

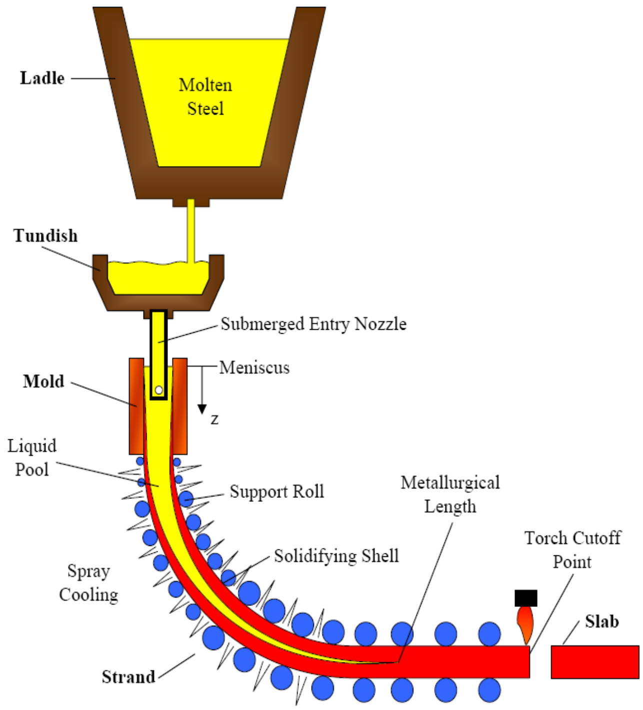

Figure.1.1 Overall Schematic of Continuous Casting Process (source: ccc.illinois.edu)

The part of the process that is of primary interest in the current project is the relationship between grains and transverse cracks that occur during formation of the cast slab from the shell in the continuous casting process. This involves modeling of the heat transfer in the mold and secondary cooling zone and analyzing the microstructure of the solidifying shell section of the strand in an efficient way to incorporate the effect external stresses as well as metallurgical effect (such as precipitates and second phase materials) on the grain boundaries.

The domain of interest is a transverse slice through the steel strand as it is solidifying while moving down the mold and below. A schematic of the domain of interest is shown in Figure.1.2. The domain is a slice of the shell as it passes down the mold and secondary cooling zone (Lagrangian frame of reference). The domain consists of columnar grains with/without precipitates that form at the grain boundaries. Appropriate boundary conditions can be enforced on the mold face wall (in terms of displacements and thermal stresses) as required for study.

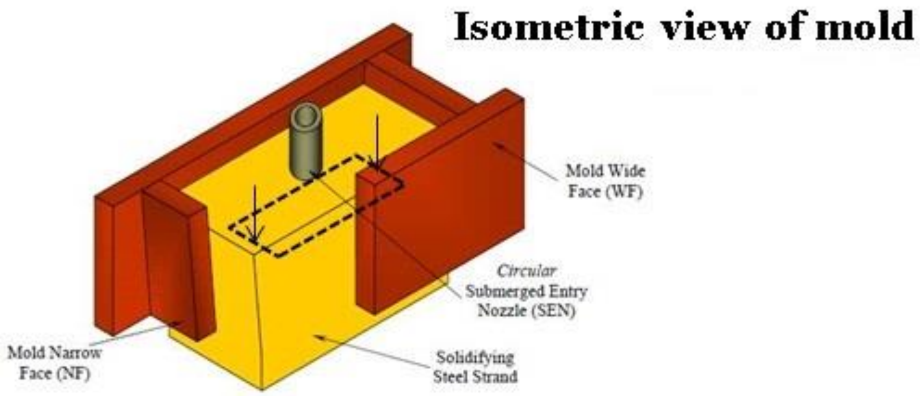

Figure.1.2 – A view from the top of mold (Hibbeler *et al* [3])

As the steel strand moves down the colder mold face, it causes the molten steel to start solidifying into a thin shell around the perimeter of the mold. This shell starts forming initially at the interface at the top of the mold and increases in thickness as the shell moves down the mold. It must be ensured that the shell as solidified to an extent such that the thickness of the shell is able to partially support itself (with help from the rollers) and the pressure exerted by the molten steel inside until the steel completely solidifies at the metallurgical length. As the steel shell solidifies (Figure.1.3), it first forms small surface grains, due to the sudden cooling of the hot molten steel as it is exposed to the mold face.

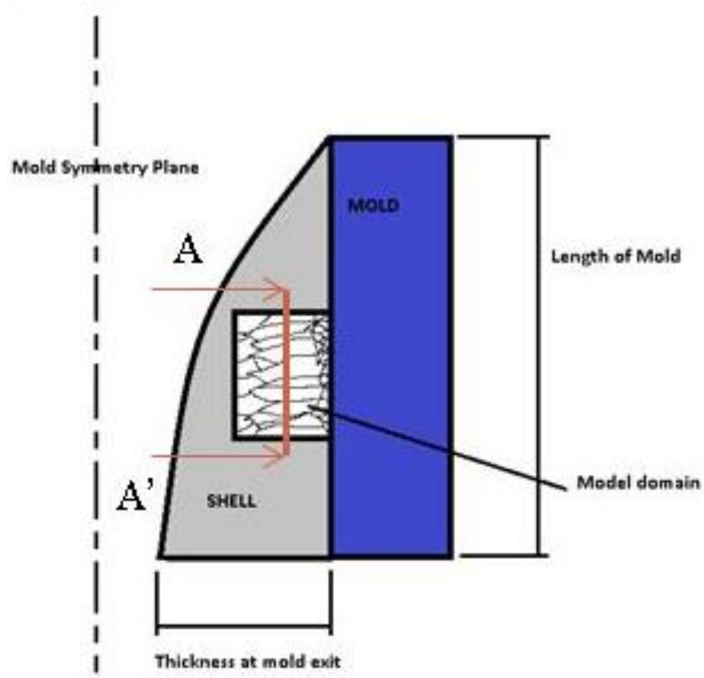

Figure.1.3. Approximate problem domain inside the mold

As the shell moves further down the mold, dendrites start forming in the solidification front. The dendrites start growing towards the central axis of symmetry of the slab from each side. These result in the formation of columnar grains of steel. These columnar grains can be several millimeters long and about a millimeter thick (Figure.1.4) [42].

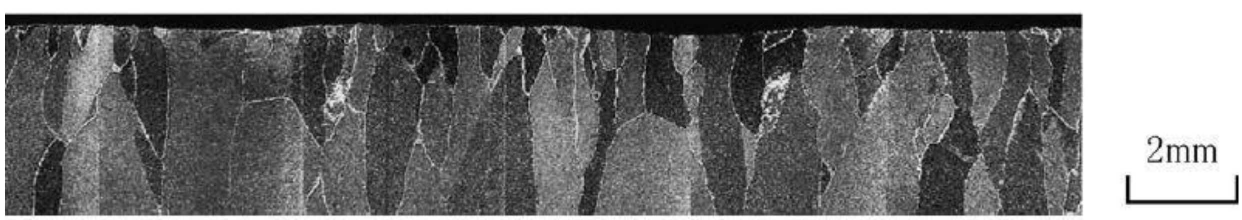

Figure.1.4. Photograph of microstructure of slab [4]

Towards the end of the solidification close the metallurgical length, equiaxed grains start forming in the central region of the slab. The present project focusses on the region with columnar grains, where most cracks form. The microstructure and behavior of the central equiaxed zone is beyond the scope of the present project and is being studied elsewhere [42] [43].

As stated earlier, the ultimate aim of the project involves controlling defects. The phenomena of heat transfer, solidification, and material kinetics as the steel cools down into columnar grain microstructure causes defects in the form of surface and internal cracks. As mentioned by Brimacombe *et al* [5], there are two fundamental requirements for the formation of cracks –

- Tensile local stresses at the grain level
- The fracture strength/strain must be exceeded in the steel

As described by Lankford [6] and as shown in Figure.1.5, external stresses related to defects occur in at least four different ways

1. Friction forces between the mold and strand
2. Thermal stresses involved in the solidification of the steel
3. Ferro-static pressure due to the liquid core of the strand
4. Unbending stresses due to straightening of the strand
5. Mechanical stresses due to misalignment of the mold and/or support rolls

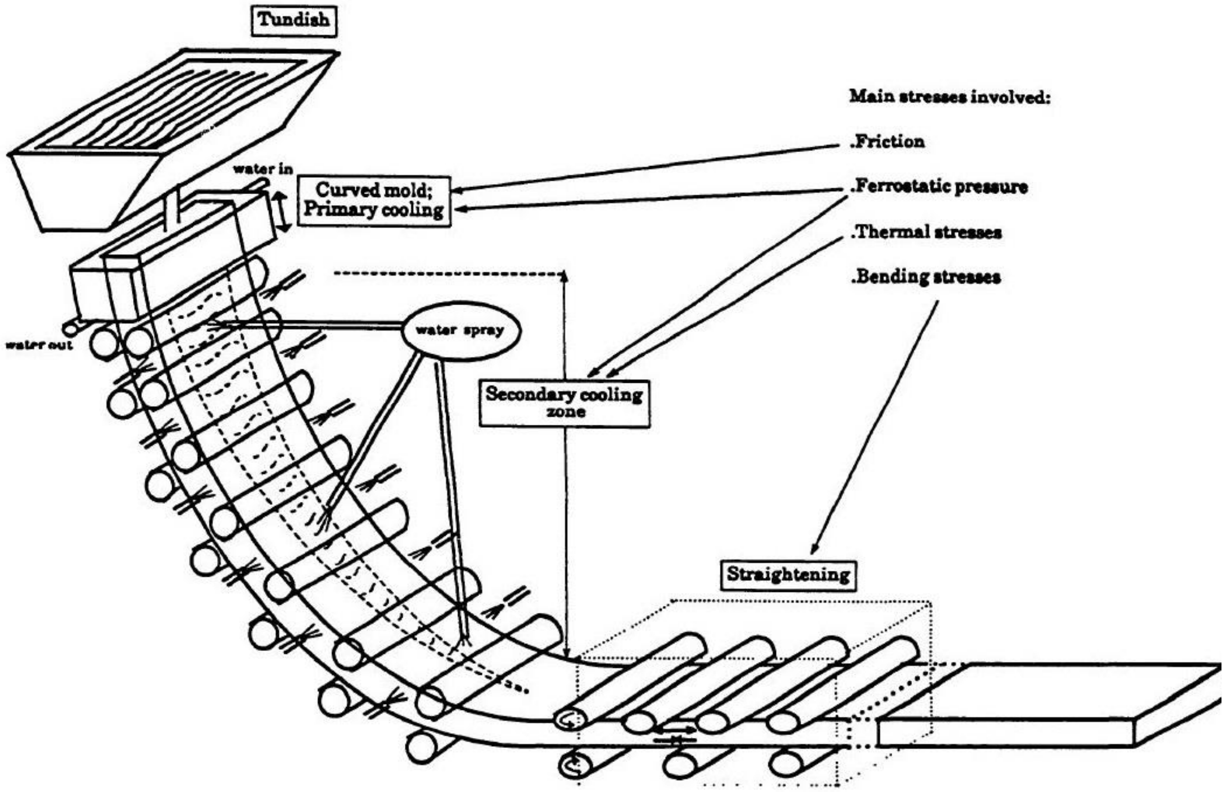

Figure.1.5. Simplified schematic of main stresses involved in a Continuous Caster [6]

These external stresses result in the formation of stress concentration in the softer regions of the steel (especially the grain boundaries and the surrounding region) which cause cracks to form. Since the strand is weakest at high temperatures, most of the cracks found in continuously cast products are generated near the mold. However, it has been noted in literature [7] that transverse cracks can also occur near the bending region due to larger stresses involved. Studies conducted by Lankford [6] suggest that the strain developed during the straightening process is around 1%-2% while strain rates of about $7x10^{-3}$ to $5x10^{-4}$ s^{-1} are typical continuous casting processes. In general, it is also known that the strains involved in a continuous caster are <5%. Hence, strains and strain rates involved in the current model will also be limited to these numbers.

Metallurgical embrittlement (regions of lower ductility due to precipitate formation leading to void growth and coalescence) is also a known condition for the formation of strain concentration leading to the formation of cracks. This embrittlement occurs due to distinct phenomena in different temperature zones of the hot steel. These are

a. <u>High temperature Zone of reduced Hot ductility (Solidus – 1340˚C)</u>

As dendrites grow at the solidification front, the steel cannot tolerate even a small strain applied. In addition, reduced ductility occurs due to micro segregation of S and P at the interface of solidifying dendrites, which lowers the solidifying temperature locally at the dendrites. This results in a reduced ductility region below the solidus where the ductility effectively reduces to zero until the inter-dendritic liquid completely freezes. Even a small strain applied while temperature is in this zone will cause cracks to propagate with the solidification front between the dendrites. These cracks then subsequently are covered or filled by enriched interdendritic fluid leading to a smooth, segregated surface in the region of failure (called hot tearing).

b. <u>Intermediate temperature zone (1100˚C – ~900˚C)</u>

At intermediate temperatures, precipitates start forming at the grain boundaries in the austenite phase, as well as inside the grains. The complex interaction of these precipitates coupled with the effect of external strain causes embrittlement and another reduced zone of ductility. Under low strain rates (10-3 s-1) embrittlement occurs at the grain boundaries due to nucleation, growth, and coalescence of voids. Application of stress also causes small precipitates to assist in the growth of these voids leading to formation of creep cavities whose densities increase. Then these cavities grow in size along the grain boundaries and coalesce leading to formation of inter-granular cracks. The action of precipitates is particularly important since they cause grain boundary pinning, which aids stress concentrations. These ultimately result in the formation of micro-cracks in the steel. At comparatively higher strain rates (10-1 s-1), these voids do not have time to nucleate and hence lead the formation of trans-granular cracks.

c. Lower temperature zone (from ~750-900˚C)

At lower temperature, (between the A1 and A3 temperatures), there is a two-phase microstructure of austenite and ferrite. This two-phase region is the primary cause of embrittlement in this temperature range. The grain boundary weakness caused by the formation of ferrite films (precipitating at the austenite grain boundaries) lead to the formation of cracks. This is because at the same temperature, ferrite is more ductile and has less strength than austenite. This can be attributed to the higher atomic diffusivity and larger number of slip systems in BCC ferrite steel compared to the FCC structure of austenite. In addition, the presence of precipitates further aggravates the problem of cracking as these aids the formation of micro-voids, which grow, coalesce, and form cracks. This mechanism is explained in Fig.4(c). The presence of a ferrite film at the grain boundary, which causes a ductile fracture at the microscale, as well as the formation of precipitates (primarily MnS or AlN) is the main cause of metallurgical embrittlement at these temperatures. The present study focusses on inter-granular cracks in this temperature zone.

The high temperature hot ductility problem, which occurs due to hot tearing, is responsible for a large variety of defects in steel except the formation of transverse cracks. The intermediate and lower-temperature zones of reduced hot ductility also account for the formation of defects in the completely solid state. The occurrence of transverse cracks is strongly correlated with the bending operations that occur in the lower end of the intermediate and lower temperature zones, which are known to result in reduced ductility (1000˚C- 700˚C). This loss of ductility is of great interest in the current work. The lower temperature zone aligns with the formation of ferrite networks on prior austenite grain boundaries (as seen in the Fe-C phase diagram (Appendix C)). With the strain concentration in these weak ferrite films at the grain boundaries further exacerbated by precipitates, studying this area of transverse crack formation is of vital interest in understanding reduction of hot ductility in the continuous casting process. Three different mechanisms have been proposed in literature for the reduced ductility due to the interaction of precipitates at the grain boundaries at these temperatures.

Suzuki et al [9] describe a mechanism shown in Figure.1.6 (a), where fine grain boundary precipitates act as stress concentrators. These fine precipitates then nucleate voids, which are aggravated by grain boundary sliding. The voids ultimately grow large enough that they begin to coalesce and form inter-granular cracks.

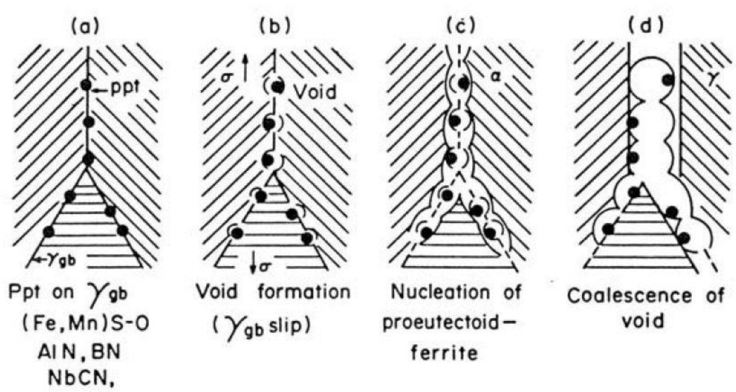

Figure.1.6 (a) – Action of precipitates as stress concentrators at austenite grain boundaries [9]

Maehara and Ohmori [10] suggest a model in which precipitation (Figure1.6 (b)) occurs simultaneously in the grain matrix as well as grain boundary. While inter-granular precipitation strengthens the matrix, the growth of grain boundary precipitates causes a depletion of particles in the proximity of the grain boundary. The softer regions around the proximity of the grain boundary (called precipitate free zones) cause strain concentration and formation of cracks in these zones.

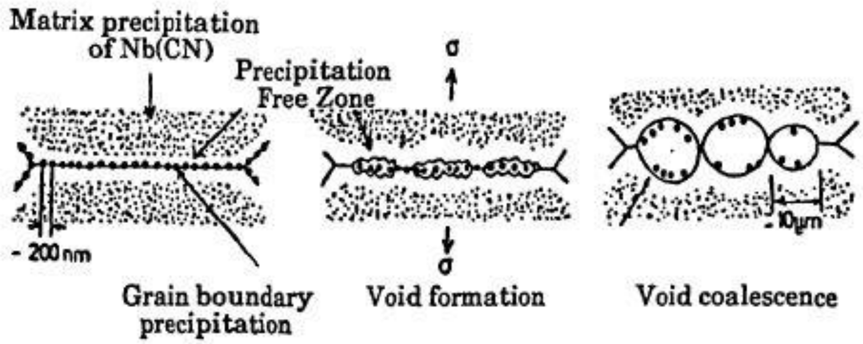

Figure1.6 (b) – Precipitate Free Zones cause cracking near grain boundary [10]

A third model developed by Yamanaka et al [11] involves the grain boundary embrittlement associated with the formation of ferrite films in the prior austenite grain boundaries causing strain to be concentrated along the softer ferrite phase (Figure1.6 (c)). This leads to formation of voids, growth of voids, coalescence and ultimately failure. Precipitates such as MnS and AlN aggravate the formation of voids and consequently aggravate the formation of cracks in the ferrite films.

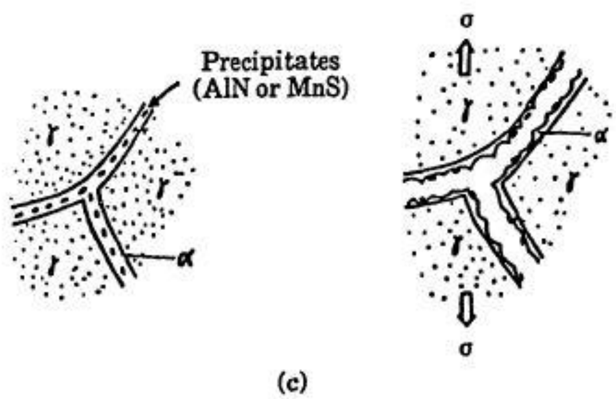

Figure1.6 (c) – Ferrite films (with/without precipitates) cause cracking near grain boundary [11]

The current model is developed drawing inspiration from the second and third embrittling mechanisms. Parameters such as strength of grain-to-grain boundary for crack initiation in the grain boundary region as well as the values of global and local strains for the failure volume fractions are obtained based on the Gurson model [1] and elastic-perfectly plastic properties for steel. In addition, certain other literature used for modeling of the steel grain and ascertaining other model properties are given as follows -

Weiner and Boley in their paper on Elasto-Plastic Thermal Stresses in a Solidifying Body [12] provide a good analytical solution for distribution of bending stresses. This result is used in the elastic- viscoplastic model developed by Hibbeler et al [14]

Brimacombe, Weinberg and Hawbolt [13] in their paper on longitudinal mid-face cracks discuss about the formation of longitudinal mid-face cracks by comparing with ductility measurements of steel at elevated temperatures of 1600°C as well as intermediate temperatures of about 1200°C to 1000˚C. A measurement of ductility as a reduction in area of cross section provides an idea of the behavior of steel at these temperatures. The effect of phosphorous on samples sensitized to steel also provides an idea on effect of precipitates in affecting the ductility of steel.

Hibbeler et al [14] in their paper on longitudinal face crack prediction with Thermo-mechanical models discuss a finite element model to simulate the thermo-mechanical behavior of the solidifying shell in a slab –caster. A commercial code ABAQUS is used to study the effect of stresses developed in a two-dimensional section of the shell as it moves through the mold. A similar mechanical model would be necessary to study the stress concentrations that develop across the grain boundaries in the presence of precipitates as well as to model the comparative weakness of grain-boundaries and their corresponding effect on crack formation.

Xu et al [15] has developed a Particle-Size grouping model for precipitation kinetics in Micro-alloyed steel. This model predicts the formation, growth, and size distribution of precipitates in the microstructure of steel. Information regarding the precipitate size and distribution can help in modeling the same in the microstructure of steel. This can then be used to predict the mechanical properties of steel using appropriate stress analysis models. While the current work does not delve into this, future work would be possible if the particle-size model and the current model are able to talk with each other during the development of the microstructure during the cooling process.

Reiter et al [16] compare indirect measurements of austenite grain size for a continuously cast slab and laboratory measurements. The results of the presented metallographic examinations serve as an important basis for the modeling of grain size and distribution for the present study.

Other important assumptions in the model are as follows. Important phenomena used in the model are the heat transfer and stress (external/thermal). In order to make the analysis easier, the phenomena involved in grain growth, precipitate formation and coarsening are left out. In addition, the heat transfer and stress analysis are uncoupled. The heat transfer using indirect techniques to ascertain temperature and then those results are used in modeling the stress in the microstructure.

In conclusion, the phenomena involved in the formation of cracks are complex and have a high correlation with the thermal-stress history. Some of the concepts involved in intermediate hot ductility need to be investigated in detail to understand the formation of cracks at these temperatures. Hence, a study of the competing mechanisms for inter-granular and trans-granular cracks is a vital piece of knowledge in further understanding of the physical phenomena important at these temperatures. The current work is aimed towards achieving some of this.

The motivations of the present work are explained from the understanding of the physical phenomena; it also fits well into the ultimate goal of the Continuous Casting Consortium. While researchers before have modeled the interplay of various physical phenomena in the continuous casting process (Figure.1.7) – from heat transfer in CON1D [40] to precipitate formation models [15], this work fits well into the last piece of the puzzle in understanding the ductility property of the steel.

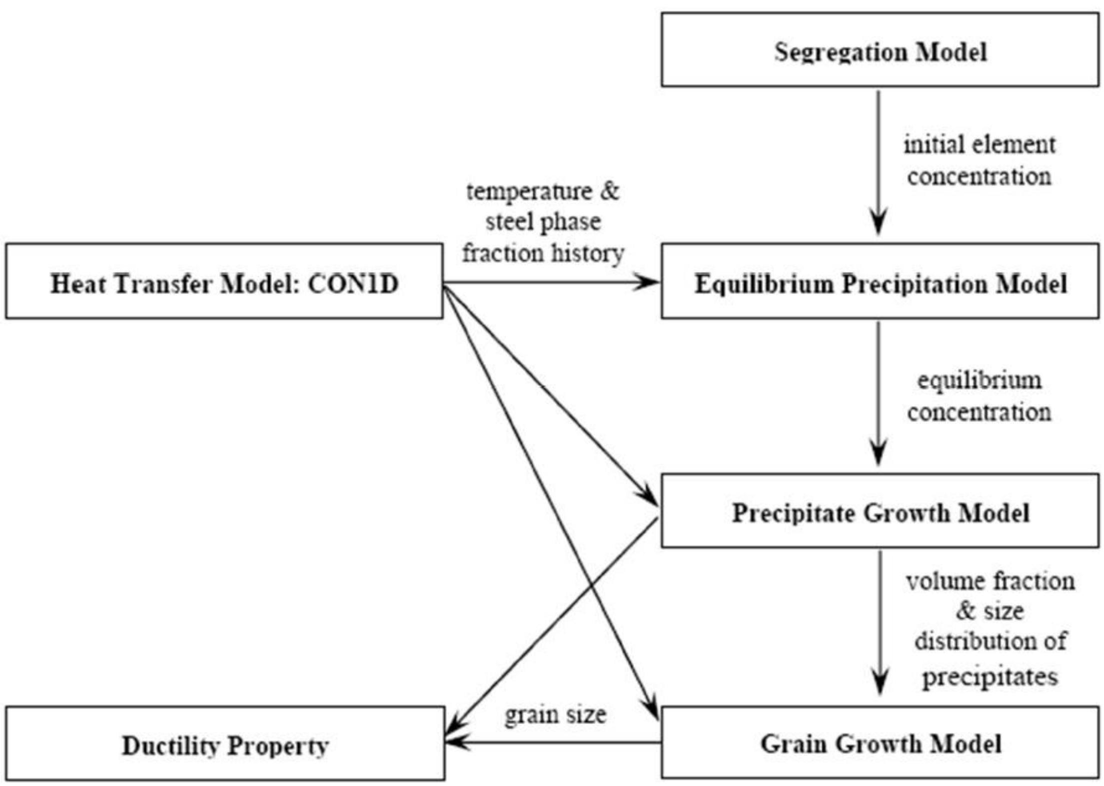

Figure.1.7 – Interacting models developed at CCC [source –ccc.illinois.edu]

1.2: FERRITE FILMS AND INTERMEDIATE HOT DUCTILITY

The mechanism of particular interest discussed in the subsequent chapters of this work involve with ferrite films that form on prior austenite grain boundaries. The crack formation in ferrite films is of interest since in the continuous casting process; this is one of the common mechanisms of embrittlement. The ferrite films form when hypo-eutectoid steel (% Carbon less than 0.76), is cooled below the Ar3 temperature of the steel (Figure.1.8). Pro-eutectoid α-Ferrite forms at prior austenite grain boundaries (Figure.1.9). These α-Ferrite (Ferrite) films are typically 10μm to 30μm thick. These ferrite films are softer and typically further weakened by formation of precipitates and lead to easy crack formation and reduction in ductility during the casting process. The temperatures at which these mechanisms are active (900°C - 750°C) making these particularly prevalent during the continuous casting process and of great interest in controlling.

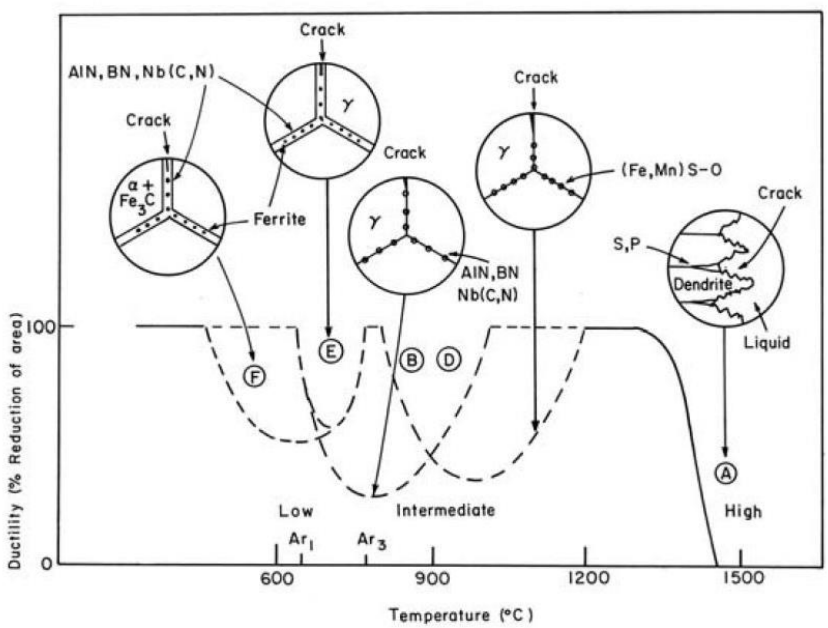

Figure.1.8 – Crack growth in ferrite films – Intermediate Hot Ductility [38]

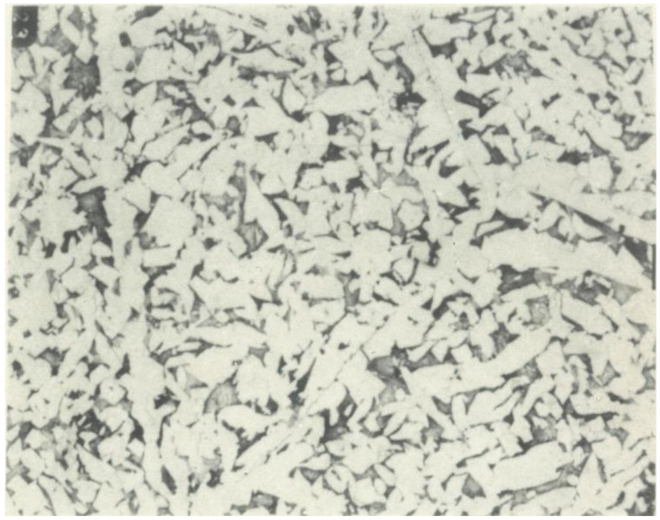

Figure.1.9 – Ferrite film formation in grain boundary of a austenite/ferrite grain [39]

When zooming further into the microstructure, as reported in the experiment that the model developed is based upon [2] [25], the embrittlement from the pro-eutectoid ferrite films on prior austenite grain boundaries can be better visualized (Figure.1.10). As these grains experience thermal stress from the casting process, there is a tendency for void formation at these ferrite films on the grain boundary (Figure.1.11). These are further exacerbated by the precipitation of the other solute elements in the alloy. Finally, these voids grow in size, coalesce and result in crack formation and embrittlement (Figure.1.12).

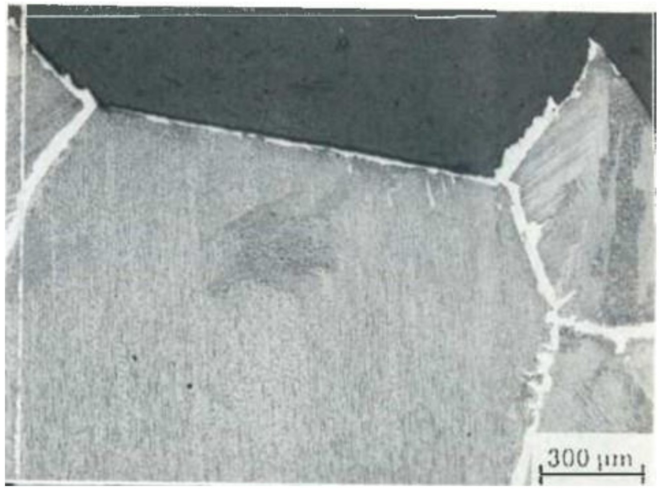

Figure.1.10 – Micro-structure of High Al steel tested at 800°C shows ferrite films form on austenite grain boundary [2]

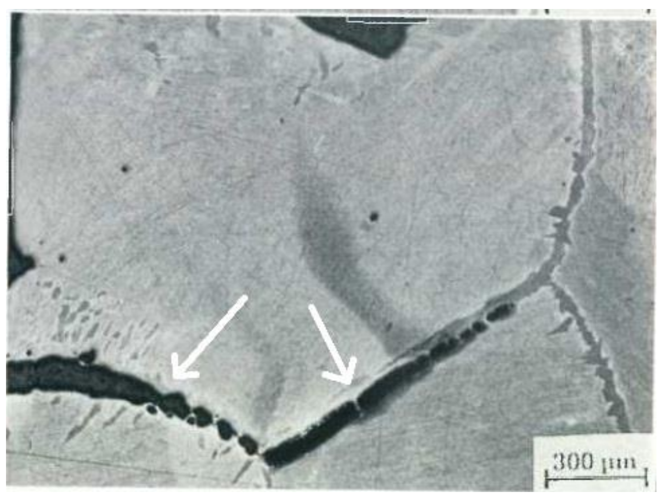

Figure.1.11 – Void formation at the grain boundaries ferrite films (white arrows) [2]

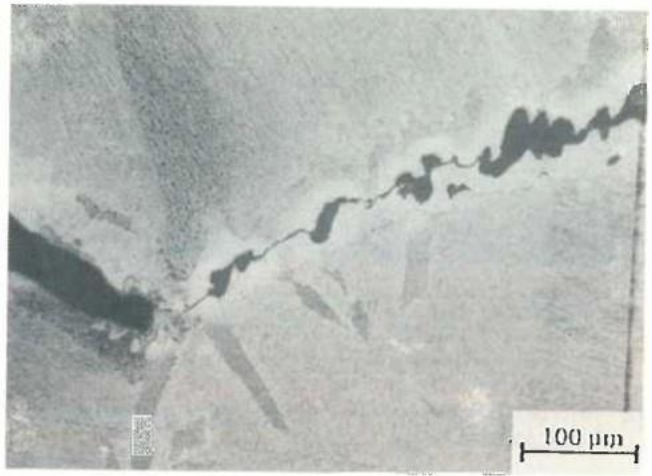

Figure.1.12 – Void linkage leading to crack formation and embrittlement [2]

CHAPTER 2: MODEL METHODOLOGY

2.1: TEST EXPERIMENT FOR MODEL VALIDATION

The first step towards developing a working computational model on intermediate hot ductility is to identify a physical benchmark experiment that can be used to validate a computational model of the phenomena. This presents a problem since there are not a lot of experiments that work with such high temperatures in the intermediate hot ductility zone 1100˚C–750˚C. Fortunately, one experiment done by Cardoso *et al* [2] fits perfectly for the present work.

The experimental setup developed by Cardoso *et al* [31] [2] describes a setup on a computerized MTS servo-hydraulic machine that can perform high temperature tensile tests. The tensile tests are performed in a protective chamber of Argon. The maximum load of the machine is 25kN and it has the capability to perform quenching of the sample upon failure as show in Figure.2.1 below – the bottom grip gives way to a hollow tube through which the bottom sample flows into a quenching container outside the protective chamber. Special heated clamps were used for holding the samples during the test the details of which this current work will not go into. Evaluation of ductility is done by measuring the reduction in area (RA) at time of fracture. The accuracy of measurement is within 3%.

Figure.2.2 (a) shows the orientation of the tensile dog-bone sample taken from along a continuous cast slab. This orientation is ideal since a tensile test taken along this direction will have the strain applied transverse to the direction of solidification growth. This simulates the straightening action of a continuously cast slab the closest – the location/time at which the formation of transverse cracks is significant. The sample was also taken from the columnar crystal zone as this minimizes the effect of surface defects or segregation that may be present in the skin of the slab.

It also avoids the center thickness regions, with non-columnar (equiaxed) grains. The thermo-mechanical cycle applied to the test piece is shown in Figure.2.3. The reheating temperature of 1350˚C ensures the dissolution of all AlN precipitates. However, at this temperature not all TiN precipitates will be dissolved [32]. The average surface cooling rate of 60K min^{-1} is used. This is similar to the surface cooling rates of a continuous cast steel slab and hence relevant to the current work. The tensile tests were performed at a constant strain rate of 10^{-3} sec^{-1} in the temperature range of intermediate hot ductility (1000˚C-700˚C).

For the current simulation model, experimental results corresponding to commercial-quality high-Al steel with the composition as detailed in Table 2.1 was chosen. This is because steel with similar compositions often experience transverse cracking in the continuous casting process. The test results examined indicated a grain size of 460μm for the austenite grains and a ferrite film thickness of 30μm. The test results at 800˚C were compared to the model, due to the relevance of this temperature in the casting process, as well as easy availability of properties.

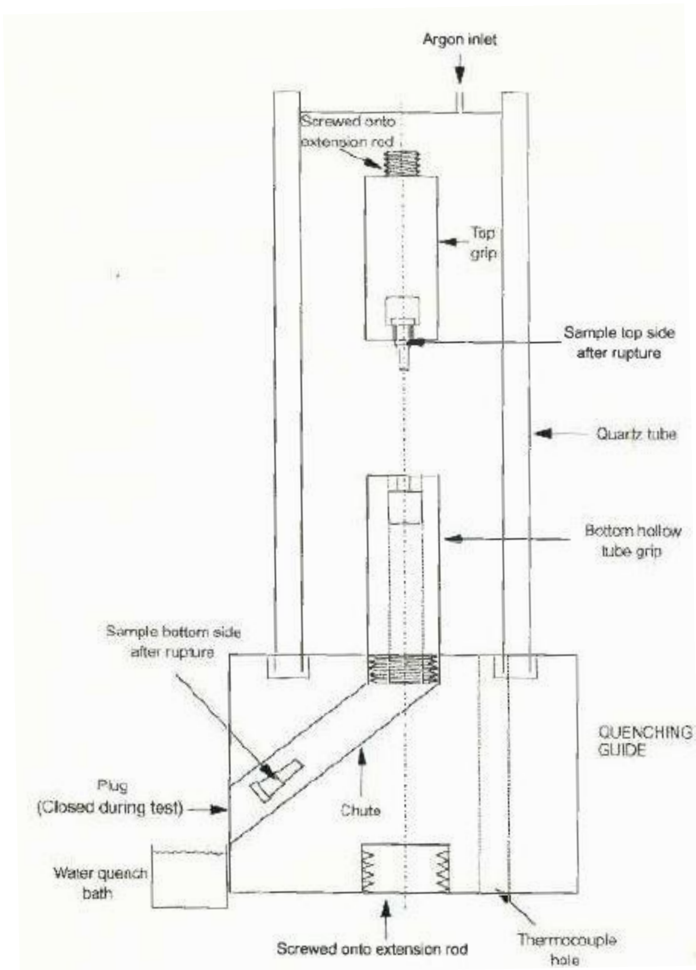

Figure.2.1 – Experimental setup [31]

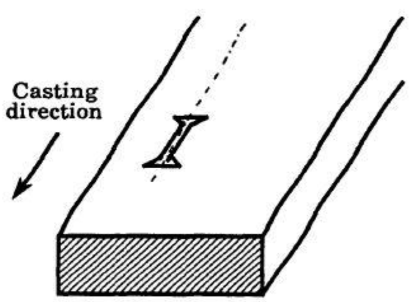

Figure.2.2 (a) Direction of sampling [2]

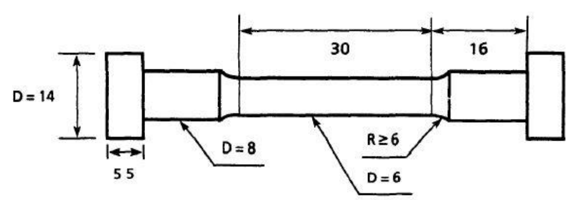

Figure.2.2 (b) Dimensions of test piece [2]

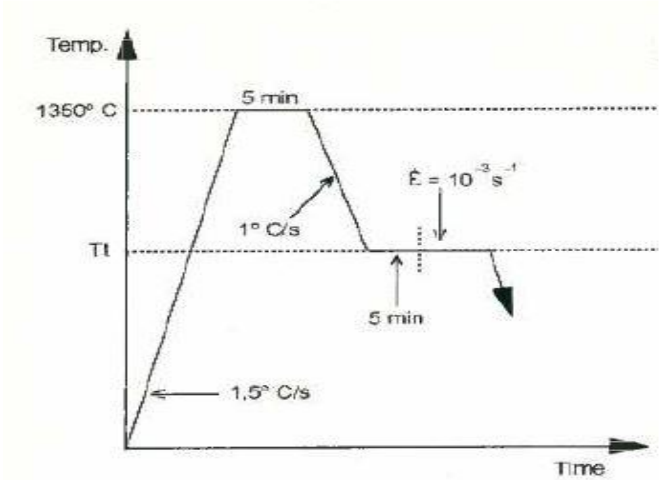

Figure.2.3 – Thermo-mechanical history of test case [31]

Table 2.1 – Composition of High-Al steel used as test case

Element	Composition (%wt.)
Carbon	0.079
Manganese	0.40
Silicon	0.019
Phosphorous	0.006
Sulfur	0.008
Aluminum	0.085
Nitrogen	0.0050

2.2: MODEL SETUP

The cast slab solidifies with a typical microstructure as shown in Figure.2.4 – a chill zone close to the surface (Narrow-Face as well as Wide-Face) with small randomly shaped grains followed by the zone with large columnar zone. The last part of the slab to solidify is the central zone of the slab (represented by molten steel in Figure.2.4). The current work focusses on the microstructure in the columnar zone because this grain structure is most susceptible to transverse cracks, primarily parallel to the Wide-face, and is relatively easy to handle geometrically in the micro-scale model.

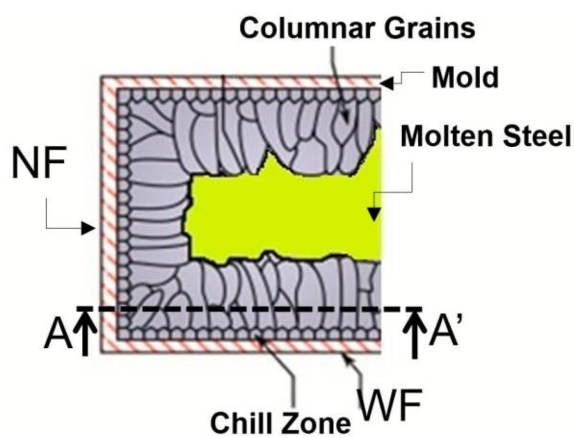

Figure.2.4 – Cross-section of a cast slab [41]

The model developed in the current work to predict steel ductility has two different scales – a micro-scale grain model capturing the microstructural behavior and a macro-model capturing necking behavior during an actual experimental tensile test [25]. The purpose of the two models is to enable modeling the microstructure behavior accurately (micro-scale) and to be able to map the results to the larger scale where experimental verification would be feasible.

For the sake of computational simplification, the large columnar grains that form in the columnar zone are approximated to a hexagonal honeycomb microstructure (looking in the solidification direction). Each columnar grain is assumed to have the shape of a regular hexagon in cross-section, and adjacent grains inter-link to form the honeycomb structure (shown in Figure.2.5). The unit cell is enclosed by the center rectangle, which contains the grain boundaries of three adjacent grains shown in blue.

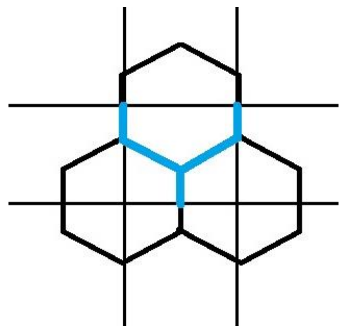

Figure.2.5 - Adjacent columnar grains

This hexagonal honeycomb structure would repeat through the columnar zone of the cast slab. Thus, a section of the columnar zone along AA' (in Figure.2.6) would present itself as regular repeating unit cells of hexagons as shown in Figure.2.6.

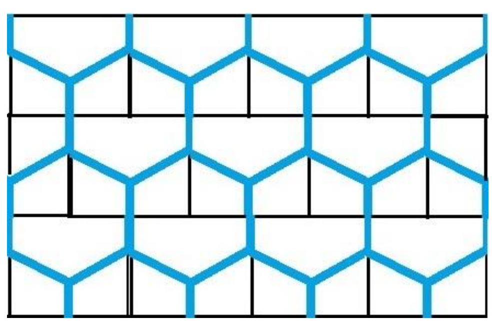

Figure.2.6 - Repeating honeycomb of hexagons

This honeycomb network can further be simplified into the fundamental repeating unit in the form of a rectangular unit cell consisting of three grain boundaries oriented at 60˚ angles, meeting at the triple point as shown in Figure.2.7. The blue areas in Figure.2.7 are the grain boundaries of the hexagonal grains, while the white areas are the interior of the grain. The black lines are the boundaries of each unit-cell in the hexagonal honeycomb network.

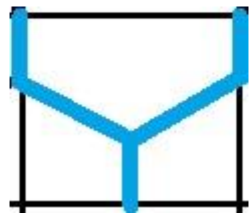

Figure.2.7 - Fundamental repeating unit-cell

Thus, the fundamental unit cell approximated to represent the columnar microstructure is as shown in Figure.2.7 with white grain matrix region and prior austenite grain boundaries consisting of ferrite films. The unit cell is periodic, so that the fundamental repeating character is able to reproduce the entire grain structure of the columnar region of the strand.

2.2.1 PERIODICITY OF GRAIN BOUNDARIES

In order for the unit cell assumption to be valid, it is essential that the periodicity (and repeating characteristic) of the unit cell is maintained. This is to ensure that any planes of symmetry present at the beginning of the deformation be maintained as the unit cell is deformed. In order to achieve this requirement, the boundaries of the unit cell need to be kept straight and parallel to the opposite side. This is achieved by using special additional boundary conditions on the boundary surfaces as detailed in Section 2.2.7.

2.2.2 GRAIN SIZE MEASUREMENT AND MODEL GEOMETRY

The microstructure in experimental data is communicated in the form of grain number, which specifies the grain size. Grain number specifically refers to the number of grains observed per unit area (usually in mm) [30]. This grain number can be related to an equivalent grain diameter [30]. For the sake of simplicity, in order to calculate the dimensions of the hexagonal unit cell in our present model, the equivalent area principle is used. With the present model consisting of a 2D slice through the microstructure, this assumes that the hexagonal unit cell is equivalent in area to a circular grain of diameter 'd' (experimental grain size). Using the geometric relationship between the length 'a' of one side of the hexagonal grain, and the area of a regular hexagon, the following relation [Equation 2.1] is derived

$$a = \sqrt{\frac{d^2 \times \pi}{6\sqrt{3}}} \qquad \text{[Equation 2.1]}$$

For a hexagon of side length 'a', the radius of an inscribed circle or "in radius", inside the hexagon, is related to the side 'a' by Equation 2.2 while the radius of the circle that circumscribes the hexagonal grain is related to side 'a' by Equation 2.3

$$\text{In-radius} = \frac{a \times \sqrt{3}}{2} \qquad \text{[Equation 2.2]}$$

$$\text{Circumradius} = a \qquad \text{[Equation 2.3]}$$

For the current test experiment that is being modeled, Cardoso et al [31] [2] describe the microstructure having a grain size of 460 μm. Using the equivalent area principle discussed above, the diameter of the grain is assumed to be 460 μm. Using Equation 2.1, then the side 'a' of the hexagon can be calculated as

$$a = \sqrt{\frac{0.460 \times 0.460 \times \pi}{6\sqrt{3}}} = 0.2529 \text{ mm} \quad \text{[Equation 2.4]}$$

Thus, the circumradius of the hexagon is 0.2529 mm while the in-radius of the hexagon can be calculated as

$$\text{In-radius} = \frac{0.2529 \times \sqrt{3}}{2} = 0.219 \text{ mm} \qquad \text{[Equation 2.5]}$$

Back calculating the ASTM standard grain number [30], this corresponds to about 6 grain/mm^2 and a grain diameter of 0.425mm (ASTM Grain number -1 and 0) [30]. This verifies that the grain size calculation is a reasonable estimation. The unit cell modeled includes three grain boundaries intersecting at a triple point and parts of the three regular hexagonal grains, which gives a rectangular shape to the unit cell (shown in Figure.2.8).

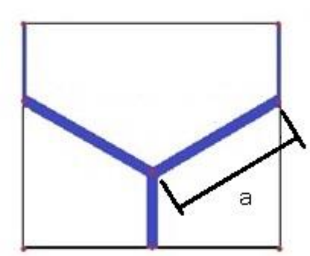

Figure.2.8 – Unit cell with location of triple point

2.2.3 DIMENSIONS OF SIMULATION DOMAIN

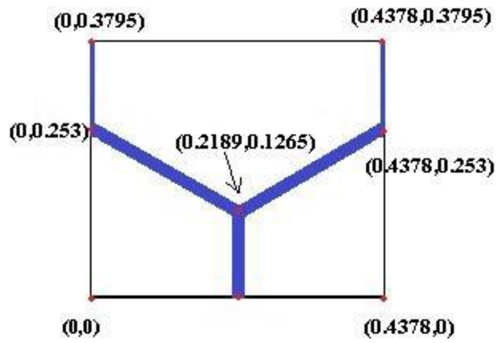

Figure.2.9 – Unit cell with location of triple point

Based on the calculations in section 2.2.3, the dimensions of the grain model domain can be calculated as shown in Figure.2.9. These are the dimensions used to create the mesh for this model. As detailed in the experiment [31], the thickness of the ferrite films is 30 μm. This is the film thickness shown in blue in Figure.2.9. The upper vertical blue regions in this figure each represent half of the ferrite film, 15μm.

2.2.4 PHASE AND MICROSTRUCTURE PROPERTIES

To account for the effect of ferrite film formation, the grain boundary region is assumed to be composed entirely of pro-eutectoid alpha ferrite, while the grain matrix region consists of prior austenite and alpha ferrite. The phase fractions are obtained from the Fe-C phase diagram [33] (Figure.2.10). Matching Cardoso's experiment temperature [3], for a temperature of 800°C, the weight percentage of the phase fractions of ferrite and austenite are obtained using the lever rule as shown in Equation 2.6 and Equation 2.7

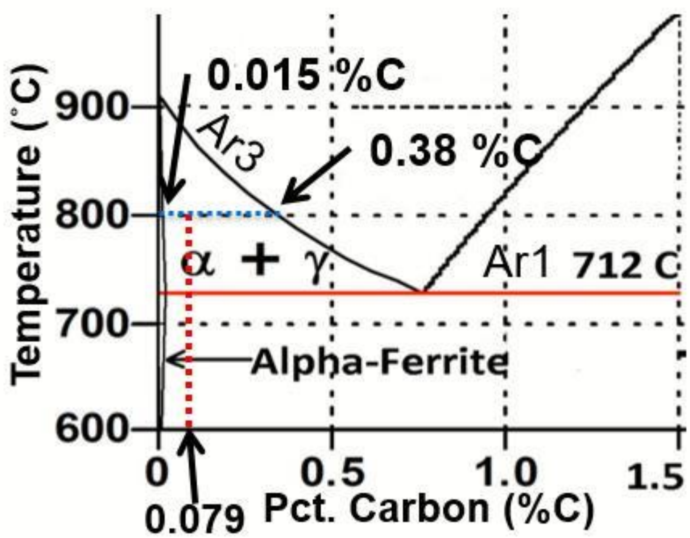

Figure.2.10 – Fe-C phase diagram showing relevant phase fractions

$$\%w_{ferrite} = \frac{0.38-0.079}{0.38-0.015} = 82\% \qquad \text{[Equation 2.6]}$$

$$\%w_{austenite} = \frac{0.079-0.015}{0.38-0.015} = 18\% \qquad \text{[Equation 2.7]}$$

Based on the phase diagram calculations, the grain matrix is composed of ~80% ferrite by weight and ~20% austenite by weight. Translating this to the geometry involves consideration of the volume of the phases. Using the relationship between the density of alpha ferrite and austenite at 800°C (temperature of experiment) [34], the weight fraction of ferrite and austenite is almost the same as the volume fraction (see Appendix A). For the sake of simplicity, the weight fraction and volume fraction are assumed the same for further development of the model for this test case.

From Figure.2.9, the total area of the domain is 0.166 mm^2. Based on the experiment observation [2] of a 30 μm thick ferrite film, the grain matrix comprises 87% of the area of the domain while the ferrite film grain boundary comprises 13% of the area of the domain. From Appendix A, assuming the weight fractions are approximately equal to the volume fractions of the ferrite/austenite, the grain matrix comprises 87% by wt. of the domain while the ferrite film grain boundary comprises 13% by wt. of the domain. The grain matrix has an 80% by wt. fraction of ferrite (@0.015% Carbon) and 20% by wt. austenite (@0.38% Carbon) (Equation 2.6 and Equation 2.7). The grain boundary region is composed of 100% ferrite films (@0.015% Carbon). Hence, the total ferrite in the domain is 80% of the grain matrix in addition to 100% of the grain boundary, which gives a total ferrite fraction of 82%. The total austenite in the domain is conversely 18%. Hence, the total carbon present in the unit cell domain is 0.08%, which is close to the value observed in the test case (Table 2.1). Hence, the phase and microstructure composition as well the volume fraction assumptions (Appendix A) are valid.

2.2.5 CONSTITUTIVE MODEL OF THE MICROSTRUCTURE

For the mechanical properties that quantify the constitutive behavior of the microstructure material, phase-dependent elastic-visco-plastic models are used. Because the timescale of the tensile test is small (in the order of minutes), creep is neglected in the analysis. While the Elastic

Modulus and corresponding Poisson ratio are obtained from data generated by Wray *et al.* [21], the plastic properties of the austenite and ferrite phases are obtained by constructing stress-strain curves by evaluating different constitutive models – Kozlowski model III [26] for austenite and Zhu power law model [27] for the ferrite. The mechanical constitutive model for the austenite consists of a stress-strain curve generated from the Kozlowski model III [26], while the mechanical model of alpha ferrite is a stress-strain curve generated with the power law formulation by Zhu [27]. The temperature dependent equations used to generate the stress strain curve plastic strength data are discussed in Appendix B (Equation B.1 and Equation B.2). These stress strain curves together define the mechanical (elastic-plastic) behavior of the model.

Table 2.2 – Mechanical properties of the microstructure

Property	Value
Elastic modulus of ferrite film	95000 MPa [21]
Poisson Ratio of ferrite film	0.3 [21]
Elastic modulus of Grain Matrix	95000MPa [21]
Poisson ratio of Grain Matrix	0.3 [21]
Plastic strength of ferrite film	Zhu model for Ferrite [27]
Plastic strength of Grain Matrix	Austenite-Kozlowski [26] & Ferrite – Zhu [27]

The behavior of the ferrite film is the same as the ferrite phase while the grain matrix is assumed to have properties similar to a composite of austenite and ferrite. The individual compositions of each phase are determined from the phase diagram and volume fractions of the film region at the grain boundary and the rest of the grain. The plastic strength of the composite grain matrix is based on Krock's rule of mixtures [28] of particle-reinforced composites where the equivalent strength of the grain matrix is the average of the upper and lower bound strengths (S).

$$S_{lower} = \frac{S_{austenite} \times S_{ferrite}}{V_{austenite} \times S_{ferrite} + V_{ferrite} \times S_{austenite}} \quad \text{[Equation 2.8]}$$

$$S_{upper} = S_{austenite} \times V_{austenite} + S_{ferrite} \times V_{ferrite} \quad \text{[Equation 2.9]}$$

$$S_{average} = \frac{S_{upper} + S_{lower}}{2} \quad \text{[Equation 2.10]}$$

where, $S_{austenite}$ and $S_{ferrite}$ are the respective strengths of the austenite and ferrite phases and $V_{austenite}$ and $V_{ferrite}$ are the volume fractions of the austenite and ferrite phases. $S_{average}$ was chosen for the stress strain relation of the grain matrix. The resultant stress vs. strain behavior is shown in Figure.2.11. This relationship is input into the model as a curve interpolated between the discrete pairs of points to define the elastic-plastic behavior for each material (ferrite film and grain matrix).

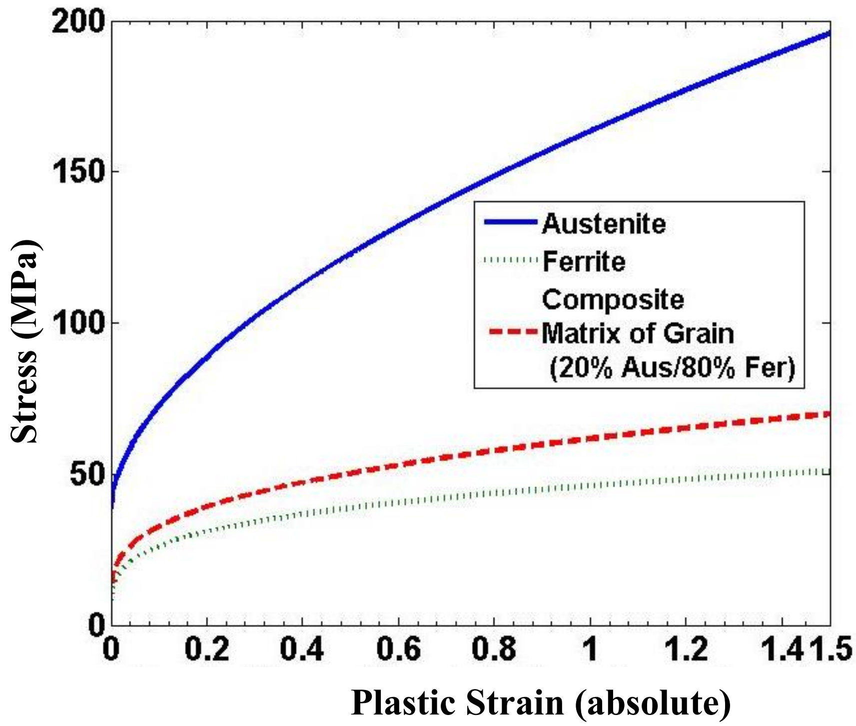

Figure.2.11 – The composite grain properties using fiber-composite equations

2.2.6 GTN MODEL FOR CRACK PROPOGATION

The Gurson-Tvergaard-Needleman (GTN) model [17] of ductile fracture was used to model fracture in the grain matrix, as well as in the grain boundary region, due to nucleation and growth of voids. In ABAQUS, which is the FEA solver platform used for this model, it is implemented as Porous Metal Plasticity Model [20].

$$\phi = \left(\frac{q}{\sigma_y}\right)^2 + 2q_1 f cosh\left(-\frac{3}{2}\frac{q_2 p}{\sigma_y}\right) - (1 + q_3 f^2) = 0 \quad \text{[Equation 2.11]}$$

Where,

$S = p\mathrm{I} + \sigma$ is the deviatoric part of the Cauchy Stress tensor σ ;

$q = \sqrt{\frac{3}{2}S{:}S}$ is the Mises stress ;

$p = -\frac{1}{3}\sigma{:}\,\mathrm{I}$ is the hydrostatic pressure

f is the volume fraction of voids

$\sigma_y(\bar{\varepsilon}_m^{pl})$ is the yield stress as a function of equivalent plastic strain $\bar{\varepsilon}_m^{pl}$

$q_3 = q_1^2$ (Tvergaard's assumption [17])

$$\dot{f} = \dot{f_{gr}} + \dot{f}_{nucl} \quad \text{[Equation 2.12]}$$

$$\dot{f}_{gr} = (1 - f)\dot{\varepsilon}^{pl}{:}\,\mathrm{I} \quad \text{[Equation 2.13]}$$

$$\dot{f}_{nucl} = \mathrm{A}\ \dot{\varepsilon}_m^{pl} \quad \text{[Equation 2.14]}$$

$$A = \frac{f_N}{s_N\sqrt{2\pi}}\exp\left(-\frac{1}{2}\left(\frac{\bar{\varepsilon}_m^{pl} - \varepsilon_N}{s_N}\right)^2\right) \quad \text{[Equation 2.15]}$$

where,

$\dot{f}$ - Total rate of change of Void fraction

$\dot{f}_{gr}$ - Rate of change of Void fraction due to void growth

$\dot{f}_{nucl}$ - Rate of change of Void fraction due to void nucleation
$A -$ Normal distribution of nucleation strain with mean ε_N and standard deviation s_N

The parameters in the Gurson model - q_1, q_2 and q_3 are 1.5, 1.0 and 2.25 for most metals according to Gurson *et al.* [17]. The other input parameters in the GTN model (f0 - initial void fraction, mean/ε_N and standard deviation/S_N of the nucleation strain distribution) were taken from Alegre *et al* [30] for austeno-ferritic stainless steels at elevated temperatures. The "volume fraction of nucleated voids" parameter, fN, was changed to 0.04 in the grain boundary region and 0.004 in the grain matrix. These model input values are tabulated in Table.2.3 and Table.2.4

Table 2.3 – GTN Model parameters in grain matrix

Parameter	Value [20][30]
q1	1.5
q2	1.0
q3	2.25
Initial void fraction, f0	0.005
Nucleation strain distribution, Mean ε_N	0.3
Nucleation strain distribution, Standard Deviation S_N	0.1
Volume fraction of nucleated voids, fN	0.004

Table 2.4 – GTN Model parameters in grain boundary

Parameter	Value [20][30]
q1	1.5
q2	1.0
q3	2.25
Initial void fraction, f0	0.005
Mean value of nucleation strain dist., ε_N	0.3
Std. dev of nucleation strain dist., S_N	0.1
Volume fraction of nucleated voids, fN	0.04

2.2.7 MICRO-SCALE MECHANICAL MODEL

The final piece of the model are the equations that drive the mechanics of the model and its implementation in the domain of interest. The isothermal model developed here operates under small strain since the steel inside the mold only experiences strains of a few percent before cracks start forming as shown by Thomas *et al.* [38]. This makes the displacement spatial gradient $\nabla u = \partial u/\partial x$ dropping the linearized strain tensor into the form in Equation 2.16 [44]. The current model being a quasi-static system, the governing force equations are defined by Equation 2.17 where, the gradient of stress tensor σ in the object is related to the body force density b. The body force, representing gravity effects, is neglected here as it is negligible relative to the mechanical forces. With a prescribed displacement on one boundary surface of the domain and a surface traction on another, this equation becomes a quasi-static boundary value problem. The total strain $\dot{\varepsilon}$ is decomposed into elastic strain $\dot{\varepsilon}_{el}$ and inelastic strain (plastic and creep) $\dot{\varepsilon}_{ie}$ (Equation 2.18) [35].

$$\varepsilon = \frac{1}{2}[\nabla u + (\nabla u)^T] \text{ [Equation 2.16]}$$

$$\nabla \cdot \sigma(\mathrm{X}) + b = 0 \qquad \text{[Equation 2.17]}$$

$$\dot{\varepsilon} = \dot{\varepsilon}_{el} + \dot{\varepsilon}_{ie} \qquad \text{[Equation 2.18]}$$

The stress σ is related to the elastic strain ε for a linear isotropic material with negligible rotations by Equation 2.19 where the elasticity tensor $\underline{\underline{D}}$ is related the shear modulus μ and bulk modulus k_B by Equation 2.20. $\underline{\underline{I}}$ and I are the fourth and second order identity tensors and ⊗ denotes the tensor product.

$$\sigma = \underline{\underline{D}} : (\varepsilon - \varepsilon_{ie}) \text{ [Equation 2.19]}$$

$$\underline{\underline{D}} = 2\mu\underline{\underline{I}} + \left(k_B - \frac{2}{3}\mu\right)\mathrm{I}\otimes\mathrm{I} \text{ [Equation 2.20]}$$

These fundamental equations for classic elastic plastic constitutive behavior are solved numerically using the Finite Element Method (FEM). The implementation of this is done using the commercial software ABAQUS 6.13-2 supported by user sub-routines using the built-in implicit Newton-based solver. The domain geometry is discretized into small elements in order to solve with the FEM method. This mesh for the micro-scale model is created in ABAQUS (See Figure.2.13).

The mechanical problem in the micro-scale domain is assumed to have a condition of "generalized plain strain" in the casting direction. This implies the out-of-plane displacement of the domain of interest is able to move due to thermal shrinkage but is constrained to follow a path that maintain straight sides with no out-of-plane bending. This assumption arises out of the fact that the two-fold symmetry of the continuous-casting strand prevents those portions of the steel shell which are above and below the plane of analysis from bending. The out-of-plane normal strain is generalized plain strain, as specified in Equation 2.21.

$$\varepsilon_{zz} = c_0 + c_x x + c_y y \quad \text{[Equation 2.21]}$$

where, c_0, c_x and c_y are constants determined as part of the solution. ε_{zz} becomes a constant with the 2-fold symmetry.

The micromodel domain is meshed with elements that consist of 6-node quadratic triangles (implemented as CPEG6H elements in ABAQUS). This mesh has 57,078 nodes and 28,332 elements. One simulation run of the microscale model had a wall clock time of around 7000 seconds on 3 Intel Xeon processors (1.8 Ghz).

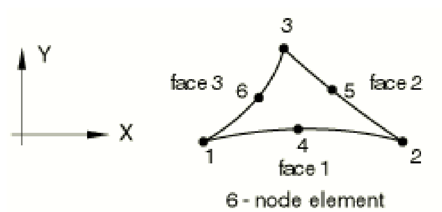

Figure 2.12 – CPE6GH elements nodes at vertex and mid-point of each triangle face [20]

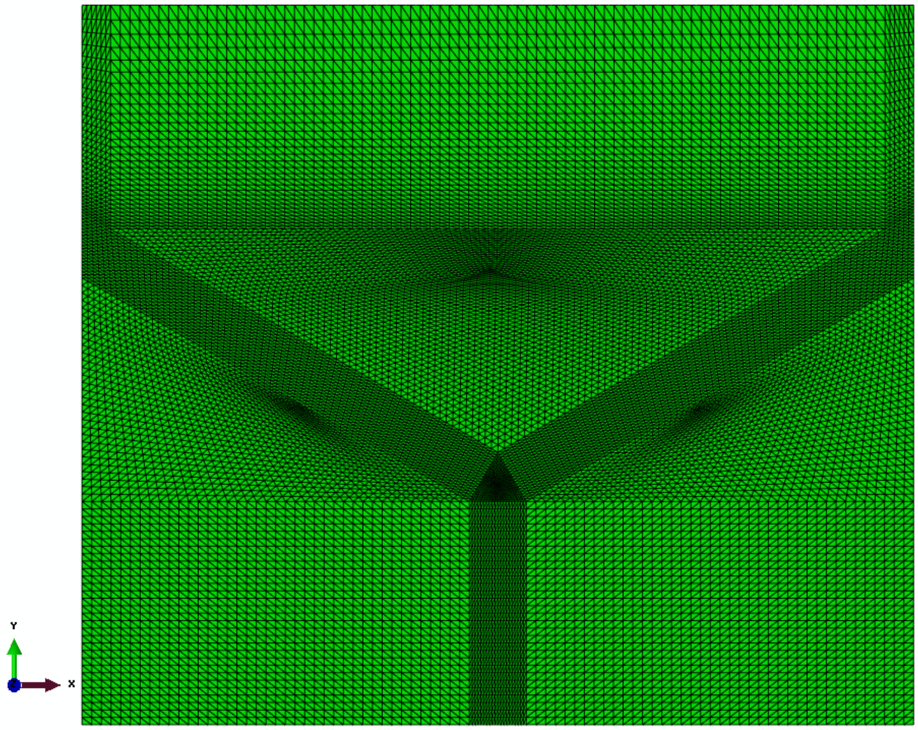

Figure.2.13 – The geometry of the meshed micro-scale model domain

In order to solve the equations for force equilibrium, suitable boundary conditions are necessary. The boundary conditions applied to the micro-model are shown in Figure.2.14. The left side of the domain is constrained to have displacement only along the Y-axis. The left-most node on the bottom surface is constrained to have displacement along the X-axis only. In order to maintain the periodicity of the domain as discussed in Section 2.2.1, additional boundary conditions are required. This is to ensure that the shape of the domain retains its repeating characteristic so that the periodicity assumption remains valid under displacement. This requires the sides to remain linear. This is enforced by two additional boundary conditions. The top boundary of the domain is constrained such that all the nodes of the mesh on the top boundary have the same displacement along the Y-axis as the left-most node. Similarly, the bottom boundary is constrained such that all the nodes on the bottom boundary have the same Y-displacement as the left-most node. These additional boundary conditions are implemented in ABAQUS using a user-defined subroutine, DISP. Since this model uses a displacement-based finite element method, the right-hand side boundary of the domain is displaced with a sufficiently large input horizontal displacement along the X-axis to induce strain, stress, crack development and propagation. The results from this mechanical model of the micro-model as well as its linking with the tensile test macro model are further discussed in Chapter 3.

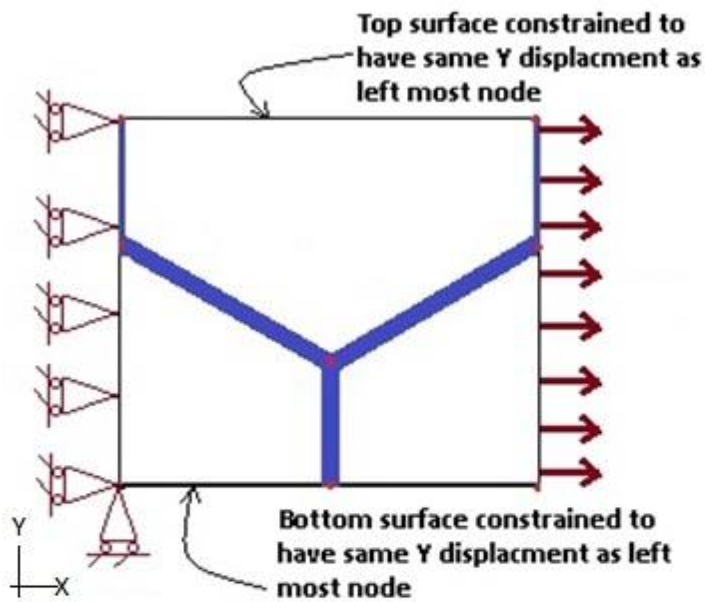

Figure.2.14 – Boundary conditions for the deflection of the unit cell under applied displacement

2.2.8 TENSILE TEST MACRO MODEL

The results from the microstructure model are ultimately compared to the experiment [2] by transforming the results of a homogenized 'effective-average' stress-strain relationship from the unit cell to a model of the tensile test specimen used in the experiment [2]. This transfer of the stress strain relationship also transfers information about the stress to crack formation at which point in the analysis, the simulation is ended.

For the tensile test model to model the tensile specimen, a similar approach is used as the mechanical model described in Section 2.2.7. A 2D axis-symmetric model is developed to simulate the benchmark experiment with the tensile specimen used by Cardoso [2] [25] with the geometry as shown in Figure.2.16. Exploiting the symmetry of the domain, only one-half of the cross-section tensile specimen needs to be modeled (solid line in Figure.2.16). Similar to the grain model, a mesh for this geometry is developed in ABAQUS with CAX4R elements as shown in Figure.2.17. The CAX4R elements use the 4-node quadrilateral shape with reduced integration first order nodes as shown in Figure.2.15 [20]

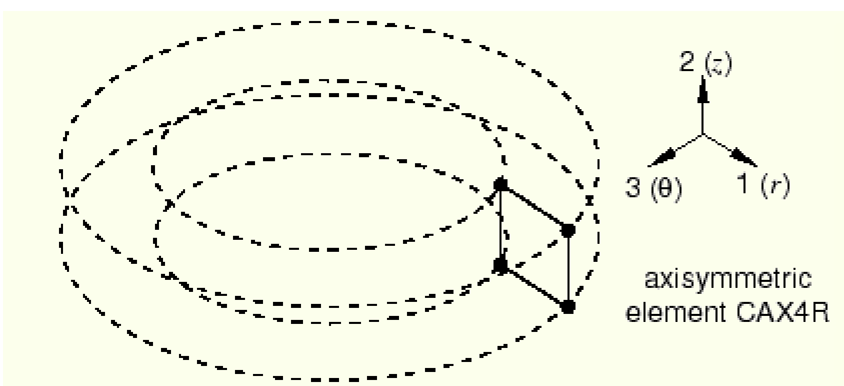

Figure.2.15 – Schematic of 4-node axisymmetric element in cylindrical coordinates [20]

The mesh has 136501 nodes and 135000 quadrilateral elements. The properties of the tensile specimen are the same as input to the grain model except for the stress-strain behavior and boundary conditions. The constitutive behavior that relates elastic strain, inelastic strain, and stress is determined from the results of the micro-model discussed in the previous sections. The smallest step size for the solver is $1x10^{-9}$ seconds while the largest step is 1 second. One simulation run of the macroscale model had a wall clock time of 30 minutes on the same three Intel Xeon processors (1.8 Ghz) used in the micro-model.

As with the micro-model, in order to solve the equations for force equilibrium, a set of boundary conditions to the macro-model are necessary. As shown in Figure.2.17, the bottom surface of the tensile specimen is constrained to have no displacement along the radial axis (X) and the vertical axis (Y). The nodes along the centerline of the specimen are constrained such that there is symmetry about the X=0 line i.e., the displacement along the radial axis as well as rotation about the vertical and azimuthal axes are zero (U1=UR2=UR3=0). The radial outside boundary of the tensile specimen is allowed to be a free edge. A vertical displacement is provided along the top boundary as defined by the test experiment described in Section 2.1. The results of the tensile test are described in detail along with the results of the micro-model in Chapter 3.

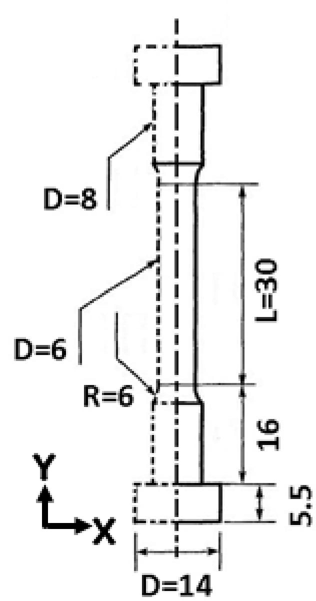

Figure.2.16 – Axis symmetric model of tensile test specimen [2]

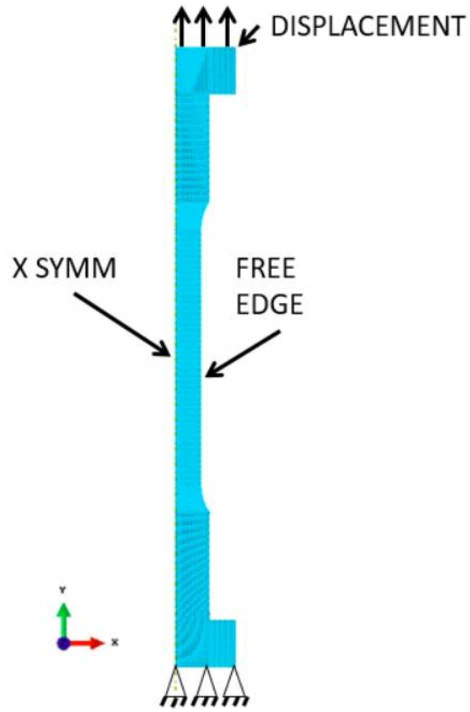

Figure.2.17 – Axis symmetric model domain of macroscale model of tensile test specimen

CHAPTER 3: VALIDATION OF MODEL

3.1 CASE A – WITH FERRITE FILMS

To simulate the experiment of the tensile specimen [30], first the micro-scale model is run, subject to an isothermal applied displacement at a strain rate of 10^{-3} sec^{-1} at 800˚C. The behavior of the unit cell obtained from this process is then used to define the plastic strength of the actual tensile specimen modeled based on the experiment.

The equivalent plastic strain from the applied displacement of the microscale model, at the instant of failure, is shown in Figure. 3.1. The maximum stress is reached at a macro plastic strain of 39% (46% total strain) at which point, the ABAQUS simulation is stopped. This deformation results in equivalent plastic strain contours, shown in Figure.3.1, where there is strong concentration of plastic strain in the grain boundary region, typical of ductile fractures. This strain concentration in the grain boundary region results in a local void fraction of 0.2, leading to crack formation. Further strain concentration from applied displacement results an increase in local void fraction up to 0.9, crack growth and failure. The final crack developed (ie at the instant of failure) can be visualized with the void volume fraction contours, shown in Figure.3.2.

In order to convert these results from the micro-scale model to the macro-scale model, there is a need to homogenize the stress vs. applied strain over the domain of the micro-scale model to obtain an averaged result. To do this, first, the Mises stress and equivalent plastic strain at each element is extracted at the element's integration point. The integration point volume of each element is also extracted using the IVOL output variable in ABAQUS. By multiplying the Mises stress (σ_{Mises}) with the IVOL parameter, a volume-weighted stress experienced by at each integration point can be calculated. The same process can be used to obtain an equivalent displacement experienced by each element by multiplying the IVOL of the respective element *i* with the equivalent plastic strain. This roughly matches the strain calculated from the displacements of the domain edges.

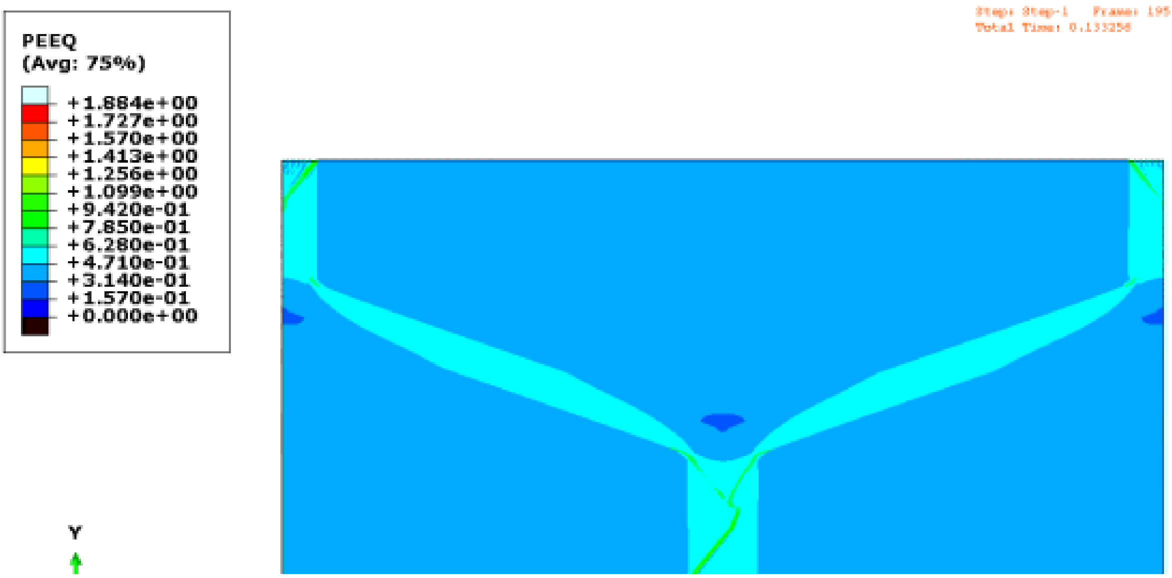

Figure.3.1 – Case A - Crack propagation in the grain boundary region under the loading

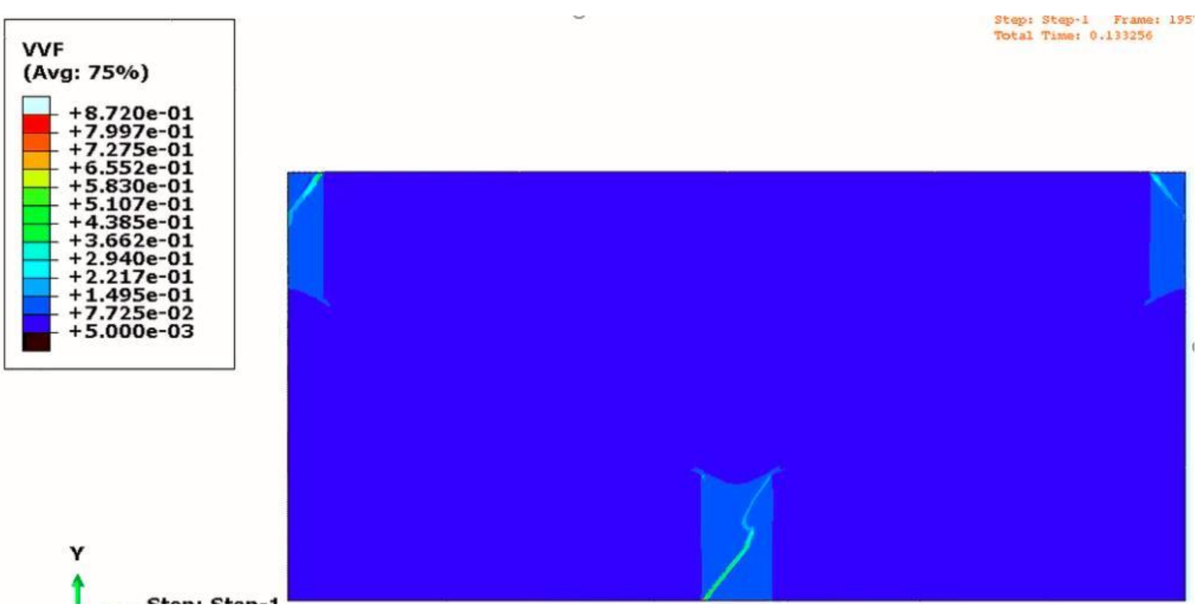

Figure.3.2 – Case A - Visualization of crack using void volume fraction in grain boundary region

By summing this elemental volume weighted stress/strain value across the entire simulation domain of the micro-scale model and dividing this with the sum of the IVOL variable over the entire domain, an overall value of the Mises stress and Strain experienced by the entire domain can be obtained. This is captured in Equation 3.1 and 3.2. By repeating this 'effective average' homogenization technique every few increments of displacement in the simulation, an overall stress vs. strain curve modelling the plastic behavior of the unit cell can be obtained as shown in Figure.3.3. Each blue point on the 'Grain model' curve in Figure.3.3 is a time-step at which this 'effective-average' technique was applied with more points sampled close to the final failure.

$$\sigma_{Mises} = \frac{1}{\sum_{domain} IVOL_i} \sum_{domain} IVOL_i \times \sigma_{i-Mises} \text{ [Equation 3.1]}$$

$$\varepsilon_{Mises} = \frac{1}{\sum_{domain} IVOL_i} \sum_{domain} IVOL_i \times \varepsilon_i \text{ [Equation 3.2]}$$

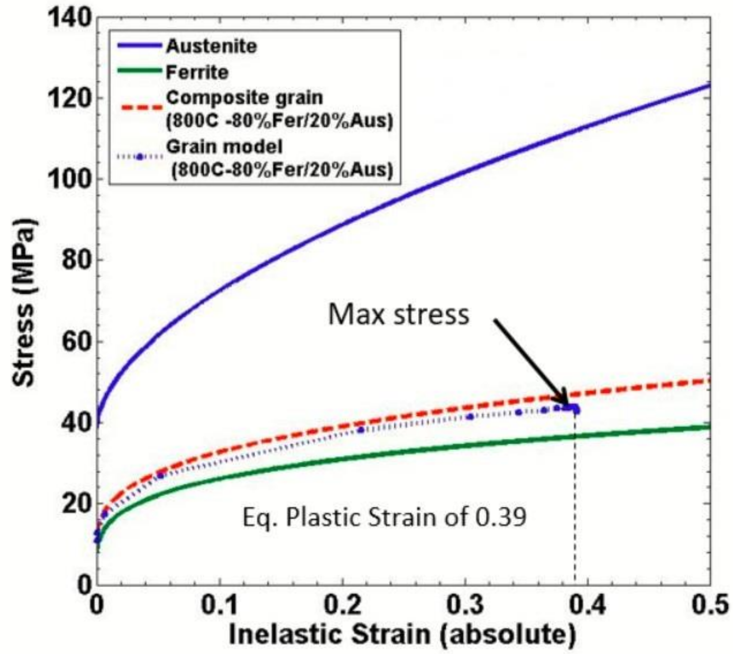

Figure.3.3 – Case A - Averaged stress-strain from the micro-scale (grain) model

This relationship is then used in the constitutive (elastic-plastic stress-strain model) relation in the macro-model of the tensile test specimen. Thus, using this hierarchical multi-scale method, information based on 'effective-average' stress from the micro-scale model is passed to the macro-model through the flow curves of Von Mises plasticity but not vice versa.

The equivalent plastic strain at failure of 39% is used to define the onset of failure of the tensile specimen. With this criterion, the macro-model tensile specimen subjected to an increasing uniaxial load. As shown in Figure.3.4, the macro-model fails at a total engineering strain of 29%, which corresponds to a 31% reduction in area, which compares reasonably with 20% reduction in area reported in the experiment.

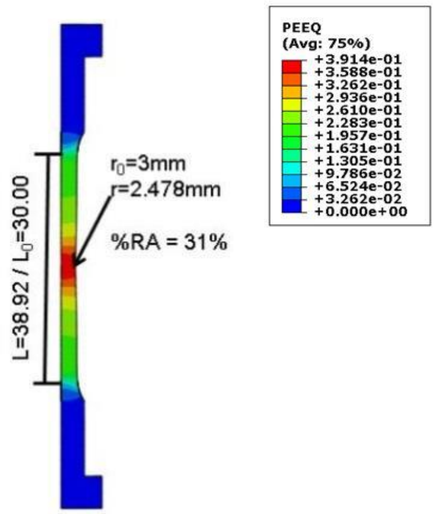

Figure.3.4 – Case A - Equivalent plastic strain at failure of macro-model as predicted by the micro-scale model

The computational model results must be compared with the results from the benchmark experiment to validate the model. This is achieved by plotting the predicted true stress vs. true strain from the macro model results of the simulation of the tensile test specimen. In order to extract the true stress vs. true strain graph, first, the engineering stress-strain data needs extracted from the macro-model. The engineering stress can be obtained from the force data along the element-nodes of a transverse cross-section of the tensile specimen. The engineering strain can be calculated by measuring the macro-strain experienced by the tensile specimen at the simulation step where the force data is extracted. From this data, the true stress and true strain data can be calculated using Equations 3.3 and 3.4.

$$\varepsilon_{tr} = \ln(1 + \varepsilon_e) \text{ [Equation 3.3]}$$

$$\sigma_{tr} = \sigma_e(1 + \varepsilon_e) \text{ [Equation 3.4]}$$

where,

$\varepsilon_{tr} = True\ strain$

$\sigma_{tr} = True\ stress$

$\varepsilon_e = Engineering\ strain$

$\sigma_e = Engineering\ stress$

The true stress vs true strain graph predict failure at 26% strain (peak in graph shown in Figure.3.5). The tensile test macro model indicates a %RA of 31% while the %RA reported in the experiment [25] is 20% (Figure.3.6). Thus, the predicted true strain for failure matches reasonably well with the measurements of the benchmark experiment [25]. However, the predicted stress to failure does not match – while the model predicts a stress to failure of 40MPa (Figure 3.6), the experimental measurement was ~10MPa (Figure 3.6). This discrepancy can be attributed to the fact that the flow strength curves (Figure 3.7) reported by Wray. P *et al.* [21], which serve as the basis for the austenite and ferrite strength input to the current model appears not to match the experimental measurements of Cardoso et al [25]. Determining the cause of this discrepancy is beyond the scope of the present work.

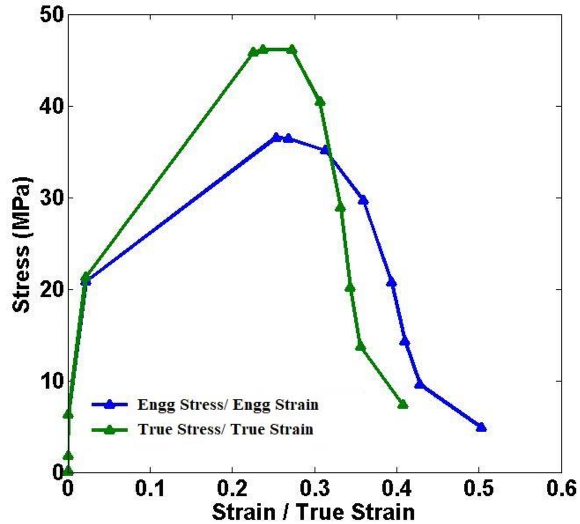

Figure.3.5 – Case A - Stress vs Strain - True strain indicates failure at 26% at a stress of 45MPa

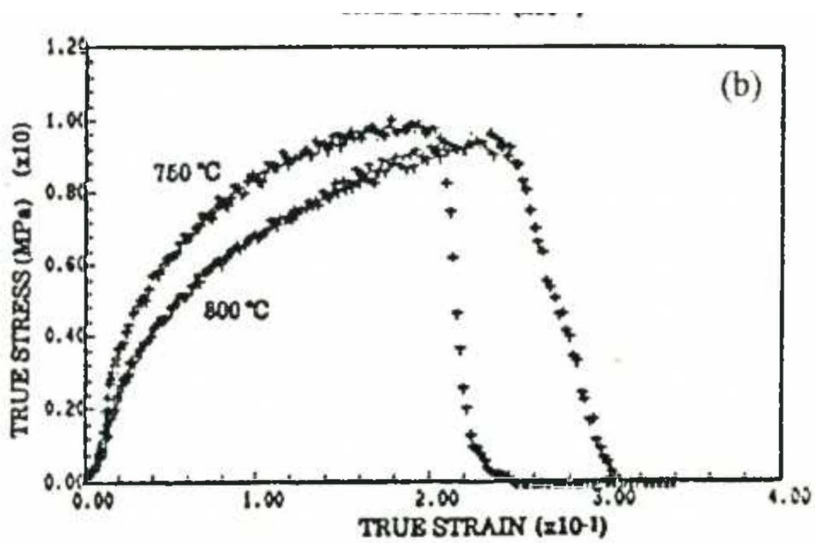

Figure.3.6 – Case A - Experimental measurements- True Stress vs True Strain [25]

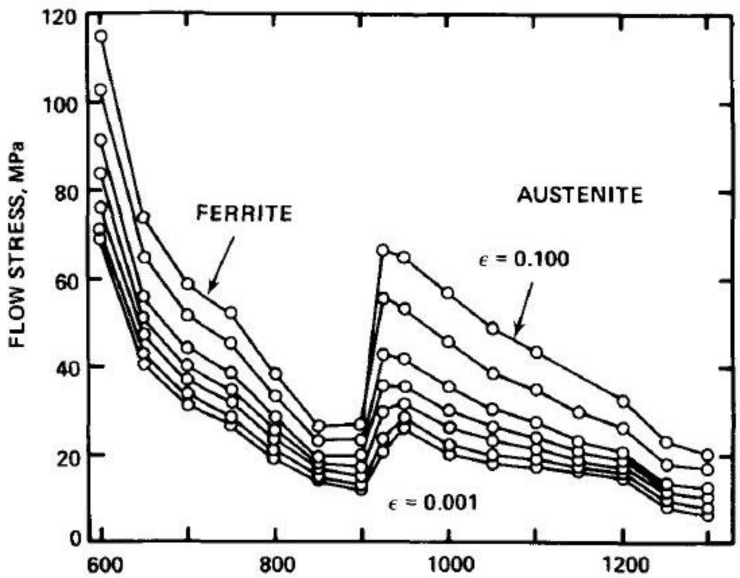

Figure.3.7 – Measured strength data (Wray. P et al) [21] used as basis for current model

3.2 CASE B – WITHOUT FERRITE FILMS

To further validate the model, the entire “micro-macro model” methodology was repeated with no ferrite films and uniform composition in the entire grain. This was done by changing the strength of the grain boundary region (blue) in Figure.3.2 to match the strength of the composite grain matrix (82% Ferrite and 18% Austenite at 800° C). This resulted in no stress concentration in the grain boundary region and the absence of embrittlement in the grain boundary region. This can be visualized in the average effective stress strain curve similar to the one in Figure 3.3 as shown in Figure 3.8. This averaged effective stress strain curve fed to the tensile specimen produces almost 100% reduction in cross-section area at necking (RA) without failure. This is expected in austenite with no embrittlement mechanism driven by ferrite films as reported by Cardoso *et al.* [25] with the low-Al steel which has excellent ductility in the absence of ferrite films at elevated temperatures of 900°C. While the high-Al steel does show poor ductility even in the absence of ferrite films at 900°C [25], Cardoso reports the fracture facets being flat indicating the failure mechanism had changed to grain boundary sliding in austenite. While, this is not a feature of the current model, it provides an opportunity for future improvement to this work. This sanity check confirms that the absence of ferrite films results in no strain concentration in the grain boundary region, which results in no premature failure of the tensile specimen and 100% reduction in area ductility, as shown in Figure 3.9

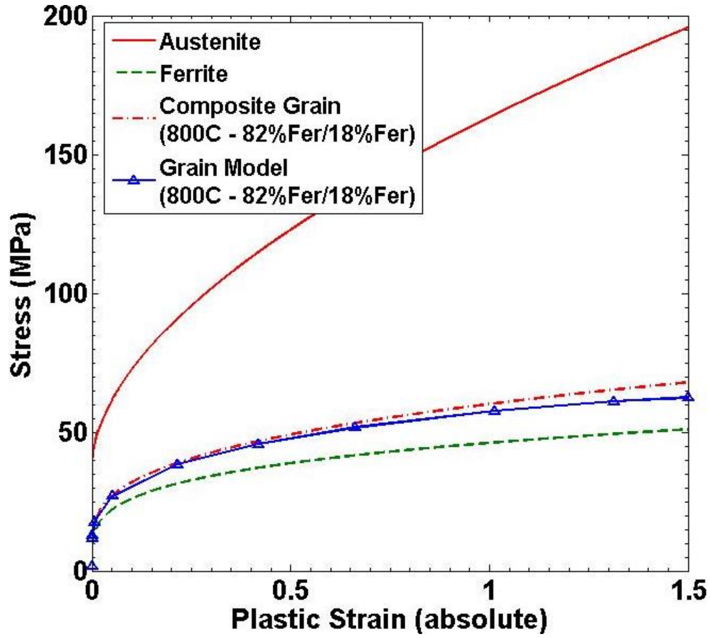

Figure.3.8 – Case B - Absence of ferrite films improve the ductility of the tensile specimen significantly

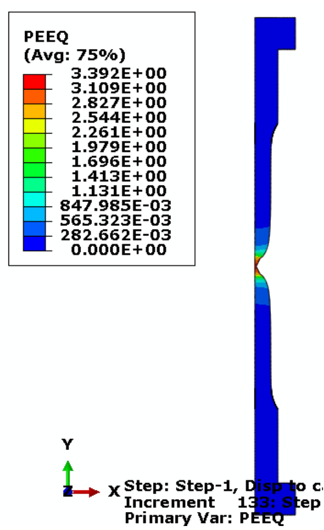

Figure.3.9 – Case B - 100% reduction in RA at necking

CHAPTER 4: PARAMETRIC STUDIES

4.1 EFFECT OF TEMPERATURE ON THE MICRO-SCALE AND MACRO-SCALE MODELS

To utilize the partially validated model developed in this work, the effect of temperature on was studied. Specifically, the micromodel simulation was repeated for increasing temperature from 800 to 870˚C. This higher temperature was chosen because at this temperature, the ratio of strength of the grain matrix to the ferrite film is twice that at 800˚C. Following the model setup from Section 2.2, the phase fractions of the micro model are recalculated at this higher temperature of interest - 870˚C. Using the lever rule (Same as Equation 2.6) and the relevant data from the iron carbon phase diagram (Appendix C), the weight fractions of the ferrite and austenite phases in the grain matrix are obtained to be:

$$\%\boldsymbol{w_{ferrite}} = \frac{0.079-0.004}{0.218-0.004} = \mathbf{35}\% \quad \text{[Equation 4.1]}$$

$$\%\boldsymbol{w_{austenite}} = \frac{0.218-0.079}{0.218-0.004} = \mathbf{65}\% \quad \text{[Equation 4.2]}$$

This means: 35% ferrite at 0.002% Carbon concentration and 65% austenite at 0.012% Carbon concentration. The ferrite films have the same concentration of carbon as the ferrite in the grain matrix. The domain and geometry, including the ferrite film thickness, was kept the same as previous (Case A). The mechanical properties used in the model are shown in Table 4.1.

Table 4.1 – Mechanical properties of the microstructure

Property	Value
Elastic modulus of ferrite film	70150 MPa [21]
Poisson Ratio of ferrite film	0.3 [21]
Elastic modulus of Grain Matrix	70150 MPa [21]
Poisson ratio of Grain Matrix	0.3 [21]
Plastic strength of ferrite film	Zhu model for Ferrite [27]
Plastic strength of Grain Matrix	Austenite-Kozlowski [26] & Ferrite - Zhu [27]

Using the same boundary conditions as shown in Figure.3.1, the averaged effective stress vs. strain relationship from the micro-scale model is plotted as shown in Figure.4.1. Failure is predicted by the microscale model at a plastic strain of 7%. The results in Figure.4.2 and Figure.4.3 show that the ferrite films fail at a much lower strain at this case of 870°C, compared to the case at 800˚C. Thus, at a higher temperature, the grain matrix has a higher-strength relative to the grain boundary, resulting in more strain concentration and failure at only 7% applied engineering macro-strain in the tensile specimen and a reduction in area of just 7%.

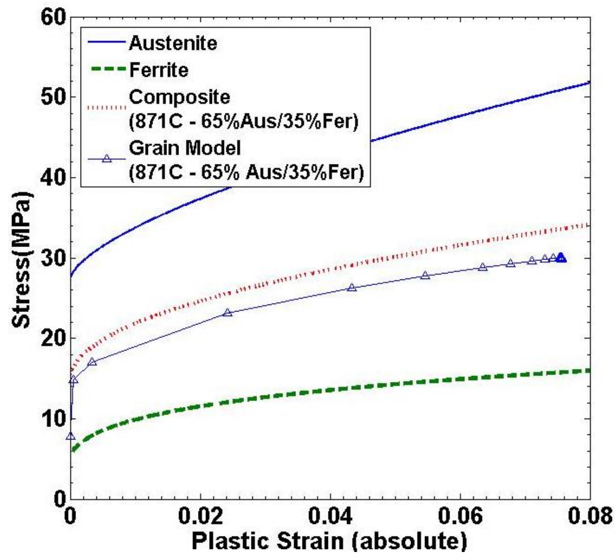

Figure.4.1– The micro-scale (grain) model indicates a void fraction of 0.2 at plastic strain of 6%

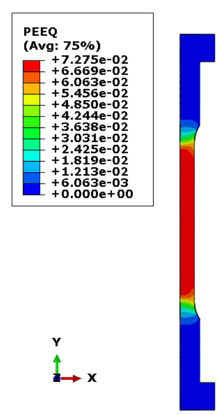

Figure.4.2– Averaged stress-strain relationship transferred to macro tensile model – %RA reduction of 6.6% at failure

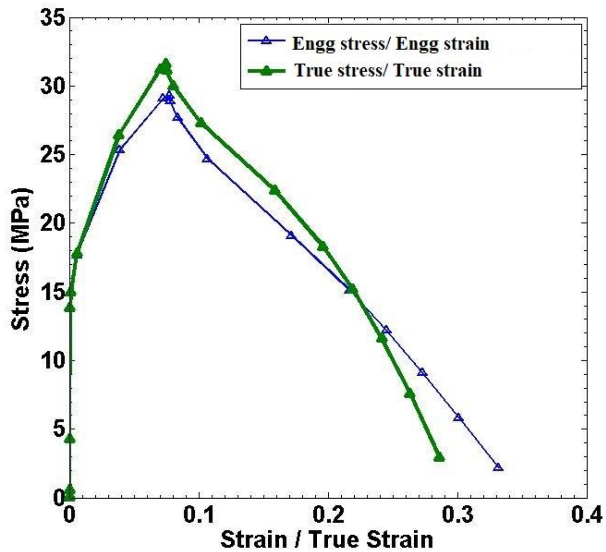

Figure.4.3– True Stress vs True Strain indicates failure at 7% at a stress of 32MPa

4.2 EFFECT OF LOADING CONDITIONS ON THE MICRO MODEL

Next, the new micro-model is applied to study the effect of loading conditions, which differ according to the location of the grains in the solidifying steel during the continuous casting process. Specifically, two new cases are studied in sections 4.2.1 and 4.2.2.

4.2.1 EFFECT OF STRAIN ALONG BOTH HORIZONTAL AND VERTICAL DIRECTIONS

The first micro model simulates grains located in a region of misalignment, where loading is experienced along both horizontal and vertical directions of the continuous-cast strand. This results in a bi-directional loading along both the directions in the plane, as shown in Figure.4.4. Other conditions, including the phase fractions, microstructure properties, and temperature of 800^{o}C, are the same as used in Validation Case 1 in Section 2.2.

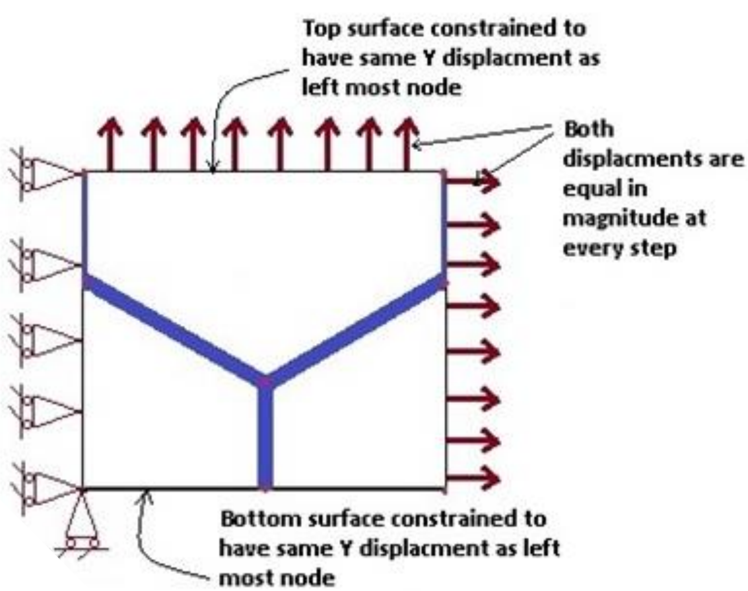

Figure.4.4–Boundary conditions for model of grain loading in misaligned region

For an applied total strain of 23%, the void growth observed is shown in Figure 4.5. Plotting the average effective stress vs. strain relationship shows an overall plastic strain of 38% at a void fraction of 0.2 (cracking). This is slightly less than the 39% plastic strain observed in the base case in Section 2.2. There is more plastic strain for applied macro-strain in this type of loading.

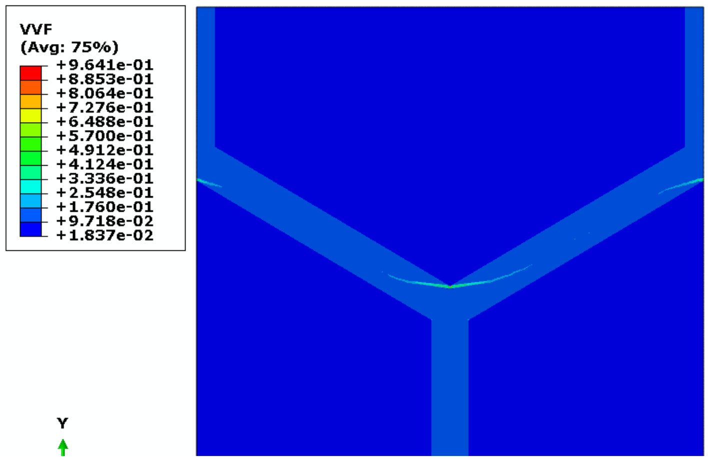

Figure.4.5– Void growth (crack propagation) for bi-directional loading

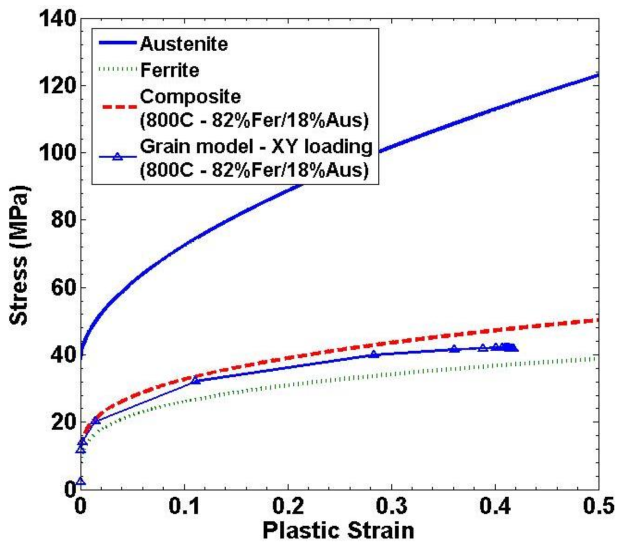

Figure.4.6– Averaged stress vs. strain relationship – Void fraction of 0.2 at 38% plastic strain

4.2.2 EFFECT OF CONSTRAINED BOUNDARY CONDITIONS

Like the bi-directional loading case studied in Section 4.2.1, a micro model simulating grains located near the corner of the continuous-cast strand was performed. With these grains being constrained by the surrounding solid metal, the boundary conditions experienced by the material in this location could be like those in Figure 4.4, where there is strain in one direction while the other three directions are constrained.

This results in strain concentration along the edge of the ferrite films and void fraction growth perpendicular to the direction of the applied load, as shown in Figure 4.8. The micro-scale model consequently predicts (as shown in Figure 4.9) a plastic strain of 36% at a void fraction of 0.2 (cracking) which is slightly less than the base case as well as the case in Section 4.2.1. This suggests that crack development may occur more easily in this condition of constrained unidirectional loading.

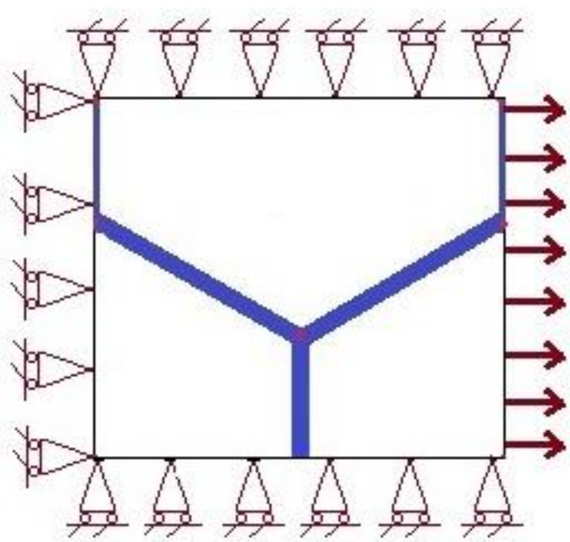

Figure.4.7–Boundary conditions for grain model of constrained unidirectional loading

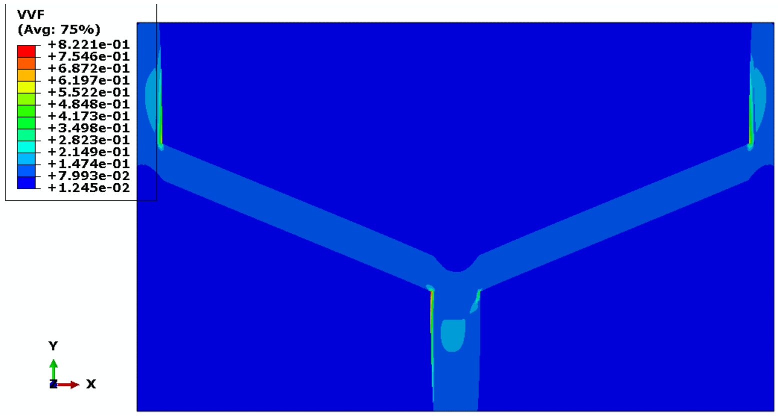

Figure.4.8– Void growth (crack propagation) for constrained unidirectional loading

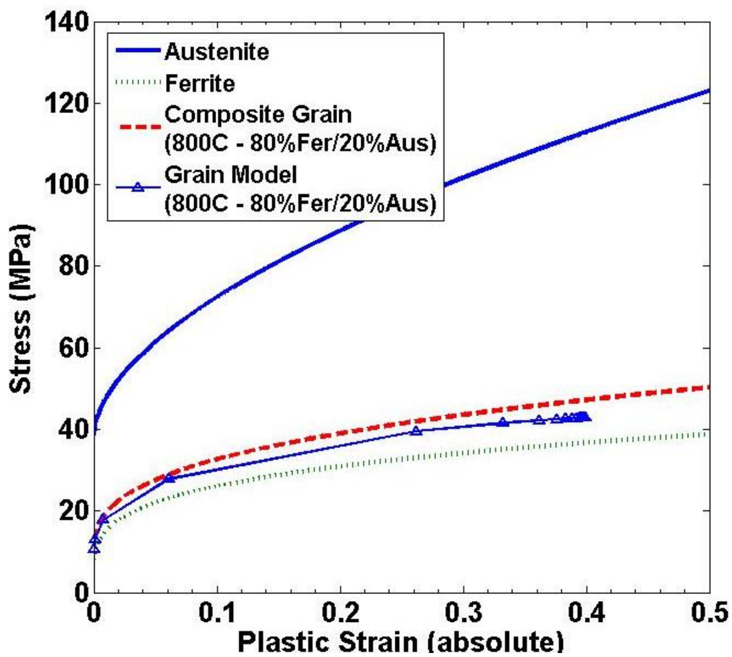

Figure.4.9– Void growth (crack propagation) for constrained unidirectional loading

CHAPTER 5: CONCLUSIONS

The continuous casting of steel is a complex process with interplay between various physical phenomena such as heat transfer, solidification, inclusion precipitation and fracture mechanics. With such a complicated interaction between different physical phenomena, tiny changes to the process do make significant changes to the quality and strength of the final product. Since the cast-steel goes onto further processing and continues to live a long life in sometimes critical applications, understanding and optimizing these processes for desired outcomes becomes essential.

In this attempt, the present work gives a framework to develop a microstructure-based methodology to analyze the hot ductility of steel. In particular, the methodology is applied to study transverse cracking that is particularly prevalent with bending operations in intermediate and low temperature zones of the continuous casting process (1000˚C- 700˚C). There are several mechanisms that have been proposed [9] [10] [11] and the mechanisms of embrittlement associated with ferrite films is the inspiration for this model. The 'particular mechanism' of ferrite films networks that form on prior austenite grain boundaries, which lead to strain concentration and exacerbate the reduction in hot ductility, is explored in detail with this model. The modeling methodology is validated against a suitable experiment performed by Cardoso *et al.* [2][25] with fairly good agreement in the %RA measure for reduced ductility. The tensile test macro model indicates a %RA of 31% while the %RA reported in the experiment [25] is 20% (Figure.3.8). However, the predicted stress to failure from the model does not match the experimental observations. In fact, with the validation case, the model over-predicts the stress to failure by a factor of four. This is due to discrepancies between the flow strength curves reported by Wray. P *et.al* [21], which serve as the basis of our model properties and Cardoso [25]. These discrepancies need further evaluation with an additional experiment, which are beyond the scope of the present work. The developed model was then used to explore the effect of temperature as well as different types of loading experienced by the micro-model as the cast strand passes through the mold. Test temperature is the main driver for the observed reduction in hot ductility as predicted by the developed model (reduction by a factor of 10). This is primarily because the testing temperature (when loading is applied) not only governs the presence or absence of ferrite films on the grain boundary but also effects the strength of the steel phases. With increase in temperature, the relative strength of the grain matrix to the ferrite films in the grain boundary region increases. This results in increased strain concentration on the weaker ferrite films leading to accelerated crack formation. Thus, maintaining the temperature of the slab accurately during crucial operations on the slab such as bending will help reduce the embrittlement due to transverse cracking. While the effect of loading on the micro-scale model (due to different locations on the strand) show different shapes of crack development, the model does not predict significant differences in hot ductility due to these. This is something that needs to be verified when the model is developed further adding more physical phenomena into it.

While there are significant assumptions made to simplify the model, these in turn make the model robust with low wall clock times. These assumptions also give further scope for expansion in the future. These are two pronged – adding new phenomena from literature that model such crack development and growth in hot ductility temperature zones as well as techniques to make the computational model more robust. One physical phenomenon that could be modeled is adding void fractions from precipitation. This feature would also help it link up with the other models developed at CCC as the final piece of the puzzle linking the chemistry of precipitation to the physics of heat transfer and continuum mechanics – robust models which already exist. This feature would also help understand the effect of void size vs. void number (indirectly relating to the size of the precipitates). Another feature that would add power to the model is the ability to model different grain sizes and ferrite film thickness as well as developing realistic microstructures using techniques such as ‘voronoi-tessalations’ than standard regular hexagons. From a computational standpoint, future work on the model can include changes to the frequency of information passage between the fine-scale (micro-scale model) to coarse-scale (macro-model) with semi-concurrent multiscale methods. These would help make the results of the model more consistent.

As a final word, this work is an attempt to explore only a miniscule portion of the complex process of continuous casting of steel. It is an attempt to build another feature into the comprehensive system of models that have been developed by previous researchers at the Continuous Casting Consortium as well as others around the world to further the understanding of this essential alloy to humanity.

REFERENCES

[1] Gurson AL. Continuum theory of ductile rupture by void nucleation and growth. Part I: Yield criteria and flow rules for porous ductile media. J Engng Mat and Techn. 1977;99: -15.

[2] G.I.S.L.Cardoso, 'The influence of microstructure on the hot ductility of four low carbon steels with respect to transverse crack formation in continuously cast slabs', Masters thesis, McGill University, 1990

[3] Hibbeler, Lance. “Thermo-Mechanical Behavior during Steel Continuous Casting in Funnel Molds.” Thesis. University of Illinois, 2009.

[4] Yasuhide OHBA, Shin-ichi KITADE and Ichiro TAKASU, Austenite Grain Refining of As-cast Bloom Surface by Reduction of Oscillation Mark Depth , ISIJ International, Vol. 48 (2008), No. 3, pp. 350–354

[5] J. K. Brimacombe and V. Samarasekera, "Fundamental Analysis of the Continuous Casting Process", In: Thermomechanical Processing of Steel, The Centre for Metall. Process Engineering, Univ. of British Columbia, Vancouver, BC, September (1989), p. 1.

[6] W. T. Lankford Jr., “Some considerations of strength and ductility in the continuous-casting process”, Met. Trans., Q, (1972), p.1331.

[7] J. K. Brimacombe and K. Sorimaehi,” Crack formation in the continuous casting of steel”, Metall. Trans. B, 8B, (1977), p. 489.

[9] H. G. Suzuki, S. Nishimura, J. Imamura and Y. Nakamura, “Characteristics of Hot Ductility in Steels Subjected to the Melting and Solidification”, Trans. Iron Steel Inst. Jpn., 24, (1984), p.169.

[10] Y. Maehara and Y. Ohmori, “The precipitation of A1N and NbC and the hot ductility of low carbon steels”, Mater. Sei. Eng., 62, (1984), p. 109.

[11] K. Yamanaka, F. Terasaki, li Ohtani, M. Oda and M. Yamashima, “Relation between Hot Ductility and Grain Boundary Embrittlement of Low-carbon Killed Steels”, Trans. Iron Steel Inst. Jpn., 20, (1980), p. 810.

[12] Weiner, J.H and Boley, B.A. “Elasto-plastic Thermal Stresses in a solidifying body.” J.Mech. Phys. Solids, 1963, Vol.11, pp.145 to 154.

[13] Brimacombe, J., F. Weinberg, and E.B. Hawbolt, “Formation of Longitudinal, Midface Cracks in Continuously-Cast Slabs.” Metallurgical and Materials Transactions, 10B:2 (1979), pg. 279-292

[14] Hibbeler, LC and Thomas, BG and Santillana, B and Hamoen, A and Kamperman, A, “Longitudinal face crack prediction with thermo-mechanical models of thin slabs in funnel molds.” LA Metallurgia Italiana, 2009, pg. 1.

[15] K. Xu and B. G. Thomas, “Particle-size-grouping Model of Precipitation Kinetics in Micro alloyed Steels,” Metallurgical and Materials Transactions A, Vol. 43A (March 2009), pg.1079-1096.

[16] Reiter. J and Bernhard. C, “Austenite grain size in the continuous casting process: metallographic methods and evaluation,” Materials Characterization, 2008, pg. 737-746.

[17] Needleman A, Tvergaard V. An analysis of ductile rupture modes at a crack tip. J Mech and Phys of Solids,1987; 35:151-83.

[18] Chu CC, Needleman A. Void nucleation effects in biaxially stretched sheets. J Engng Mat and Techn 1980; 102:249-56.

[19] Foster Wheeler Corporation, “Intermediate Heat Exchanger for Fast Flux Test Facility: Evaluation of the Inelastic Computer Programs,” report prepared for Westinghouse ARD, Foster Wheeler Corporation, Livingston, NJ, 1972.

[20] ABAQUS 6.10 Online USER manual – Benchmarking problems.

[21] Wray, P.J. “Effect of Carbon Content on the Plastic Flow of Plain Carbon Steels at Elevated Temperatures.” Metallurgical Transactions A, Vol. 13A, January 1982, Pg.125-134.

[22] G. Bernauera, W. Brocksa, W. Schmitt, "Modifications of the Beremin model for cleavage fracture in the transition region of a ferritic steel", Engineering Fracture Mechanics 64 (1999) 305-325.

[23] Hardin, R.A., Beckermann, C., “Effect of Porosity on Deformation, Damage and Fracture of Steel,” Research Report.

[24] Mintz et al, “Hot ductility of steels and its relationship to the problem of transverse cracking during continuous casting,” International Materials Reviews 1991 Vol. 36 No.5 187.

[25] G.I.S.L Cardoso, B. Mintz and S. Yue, 1995, “Hot ductility of aluminum and titanium containing steels with and without cyclic loading temperature oscillations” in Ironmkg & Steelmkng, 22-5,365-377.

[26] P.F. Kozlowski, B.G. Thomas, J.A. Azzi, and H. Wang, 1992, “Simple constitutive equations for steel at high temperature” in Mat. Transactions 23A, 903-918.

[27] Zhu H., 1993, “Coupled thermal-mechanical FE model with application to initial solidification", Ph.D. Thesis, University of Illinois.

[28] R. H. Krock, 1963, "Effect of Composition and Dispersed-Phase Particle-Size Distribution on the Static Elastic Moduli of Tungsten-Copper Composite Materials" in ASTM Proceedings 63, 605-12.

[30] J. M. Alegre, J. Perez, F.Gutierrez-Solana and L. Sanchez, 2000, ”The application of Gurson-Tvergaard Needleman model in the age embrittlement of austeno-ferritic stainless steels” in Proceedings of ECF 13, San Sebastian, Spain.

[30] ASTM Handbook Ed4

[31] G.I.S.L Cardoso, B. Mintz, and S. Yue, ‘Hot ductility of aluminum and titanium containing steels with and without cyclic loading temperature oscillations’, Ironmaking and Steelmaking, 1995, Vol.22,No.5,Pg365-377

[32] K.Narita, “Physical chemistry of the groups IVa (Ti, Zr), Va (V, Nb, Ta) and the rare earth elements in steel”, Trans. Iron Steel Inst. Jpn Journal Volume: 15:3, Mar 1975, Pg.145-152

[33] Iron-Carbon phase diagram from - www.calphad.com/iron-carbon.html

[34] Li, Chunsheng and Thomas, BG, “Thermomechanical Finite-Element Model of Shell Behavior in Continuous Casting of Steel”, Metallurgical and Materials Transactions B, Vol.35B, December 2004, pg.1151-1172

[35] S. Koric and B.G. Thomas, “Efficient Thermo-Mechanical Model for Solidification Processes” in International Journal for Num. Methods in Eng. 66, 2006, 1955-1989.

[36] Wray, P.J. “Effect of Carbon Content on the Plastic Flow of Plain Carbon Steels at Elevated Temperatures.” Metallurgical Transactions A, Vol. 13A, January 1982, Pg.125-134

[37] Wray, P.J. “High Temperature Plastic-Flow Behavior of Mixtures of Austenite, Cementite, Ferrite, and Pearlite in Plain-Carbon Steels” Metallurgical Transactions A, Vol. 15A, November 1984, pg.2041-2058

[38] B.G.Thomas, J.K.Brimacombe, and I.V.Samarasekara,”The Formation of Panel cracks in Steel Ingots: A-State-of-the-Art Review”, ISS Transactions, 1986, Vol.7, Pg. 7-20

[39] B.G. Thomas, PhD Thesis, University of British Columbia, 1985

[40] Ya Meng and Brian G. Thomas, “Heat transfer and solidification model of continuous slab casting: con1d”, Metallurgical and Materials Transactions B, Vol. 34B, No. 5, Oct., 2003, pp. 685-705.

[41] https://commons.wikimedia.org/wiki/File:Cast_ingot_macrostructure.svg under license Creative Commons

[42] Szekeres, E.S., “A Review of Strand Casting Factors Affecting Transverse Cracking”, Proceedings of the 6th International Conference on Clean Steel, Balatonfüred, Hungary, 10-12 June 2002, OMBKE, Budapest, 324-338

[43] Toru Kato, Yoshiki Ito, Masayuki Kawamoto, Akihiro Yamanaka and Tadao Watanabe, “Prevention of Slab Surface Transverse Cracking by Microstructure Control”, ISIJ International, Vol. 43 (2003), No. 11, pp. 1742–1750

[44] Mase, G.E., Mase, G.T., 1999. Continuum Mechanics for Engineers, 2nd ed. CRC Press.

APPENDIX A – WEIGHT VS. VOLUME FRACTIONS

Relationship between weight and volume fractions of alpha ferrite and austenite at 800°C (test temperature, T) – The values of weight and volume fraction are close and hence the extra step of calculating weight fractions can avoided [34].

Where,

$\rho_\alpha = density\ of\ alpha\ ferrite$

$\rho_\gamma = density\ of\ austenite$

$\%wt_\alpha = \%Weight\ fraction\ of\ alpha\ ferrite$

$\%wt_\gamma = \%Weight\ fraction\ of\ alpha\ ferrite = 100 - \%wt_\alpha$

$$\rho_\alpha\left(\frac{kg}{m^3}\right) = 7881 - 0.324 \times T(°C) - 3 \times 10^{-5} \times T^2(°C) \quad \text{- Equation A.1 [34]}$$

$$\rho_\gamma\left(\frac{kg}{m^3}\right) = \frac{100 \times (8106 - 0.51 \times T(°C)}{(100 - (pct\ C)) \times (1 + 0.008 \times (pct\ C))^3} \quad \text{- Equation A.2 [34]}$$

$$\rho_\alpha\left(\frac{kg}{m^3}\right) = 7881 - 0.324 \times 800 - 3 \times 10^{-5} \times 800^2 = 7602.6\left(\frac{kg}{m^3}\right)$$

$$\rho_\gamma\left(\frac{kg}{m^3}\right) = \frac{100 \times (8106 - 0.51 \times 800)}{(100 - (0.079)) \times (1 + 0.008 \times (0.079))^3} = 7689.58\left(\frac{kg}{m^3}\right)$$

$$\%wt_\alpha = \frac{0.82 \times 7602.6}{0.18 \times 7689.58 + 0.82 \times 7602.6} = 81.8\%$$

APPENDIX B – KOZLOWSKI AND ZHU MODELS

COMPARISON BETWEEN EXPERIMENTAL DATA AND KOZLOWSKI- ZHU MODELS

For modelling the plastic strain in the grain models, the Kozlowski and Zhu models have been used in austenite and ferrite phases. In order to test the validity of these models, they were studied against interpolated data from P. Wray [36]. For this analysis, a test temperature is 920°C is picked. 920°C is above the temperature for start of austenite to ferrite transformation (912°C). At this temperature, the microstructure should consist of Austenite only. Hence, this data from experiments by P.Wray (for a similar %C) are compared with the Kozlowksi model at this temperature to verify the validity of using these properties. P.Wray's extrapolated data matches well with the Kozlowski model for Austenite at this temperature match well thus validating that using the model for modelling the stress-strain relationship in austenite.

$$\dot{\bar{\varepsilon}}_{ie}\ [sec^{-1}] = f_c\ (\bar{\sigma}\ [MPa] - f_1 \bar{\varepsilon}_{ie} |\bar{\varepsilon}_{ie}|^{f2-1})^{f3} \exp\left(-\frac{Q}{T[K]}\right) \qquad \text{[Equation.B.1]}$$

Kozlowski model III [34]

Where :

Q = 44,465

$f_1 = 130.5 - 5.128\times10^{-3}\ T\ [K]$

$f_2 = -0.6289 + 1.114\times10^{-3}\ T\ [K]$

$f_3 = 8.132 - 1.54\times10^{-3}\ T\ [K]$

$f_c = 46{,}550+71{,}400(\%C)+120{,}000(\%C)^2$

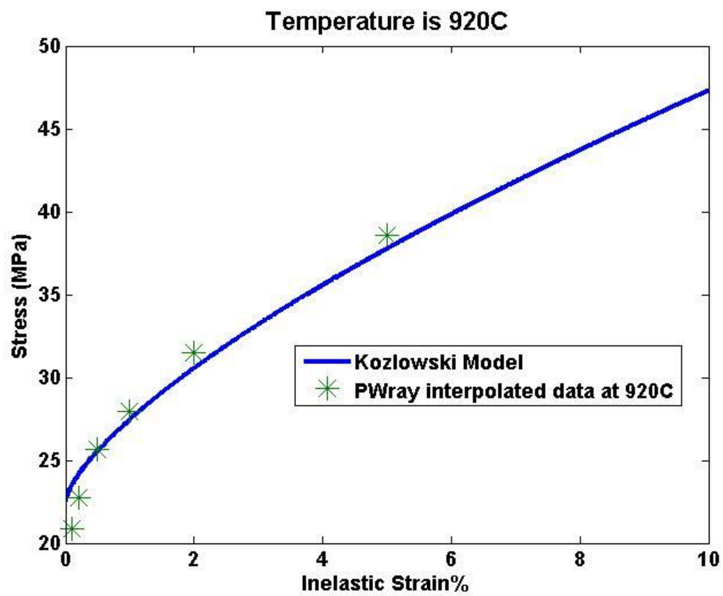

Figure.B.1. Kozlowski model plotted against interpolated data for austenite

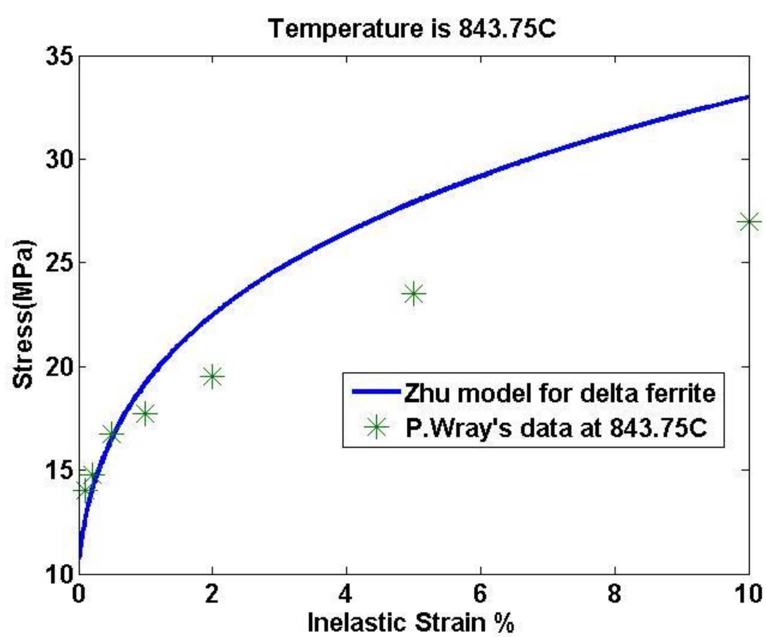

Figure.B.2. Zhu model plotted against interpolated data for ferrite

$$\dot{\bar{\varepsilon}}_{ie}[sec^{-1}] = 0.1 \left| \frac{\bar{\sigma}\ [MPa]}{f_{\delta c}\ (\%C)\left(\frac{T[K]}{300}\right)^{-5.52}(1+1000\ \overline{\varepsilon_{ie}})^{m}} \right|^{n} \text{ Equation.B.2.}$$

Zhu Power Law model [27] [34]

Where:

$f_{\delta c}$ (%C) = 1.3678×10^{4} (%C) $^{-5.56\ \times 10\text{^}-2}$

m = -9.4156×10^{-5} T [K] + 0.3495

n = $\frac{1}{1.617 \times 10^{-4}\ T\ [K] - 0.06166}$

A similar analysis is also done comparing Zhu's model for delta ferrite with P. Wray's [37] data for a similar grade (0.007 %Carbon) steel at 845˚C. At this temperature and this carbon content, the phase is predominantly Alpha Ferrite. Hence, a comparison can be made with the Zhu model. While there is reasonable agreement at low value of percent inelastic strain, the model diverges from the data at higher value of inelastic strain. The RMS error between Wray's data and Zhu's model is 1.18 MPa.

APPENDIX C – IRON CARBON PHASE DIAGRAM

FE-C phase diagram [33]